BAMS Article

Fatima-GB: Searching Clarity within Marine Fog

H. J. S. Fernando,[a] C. Dorman,[m] E. Pardyjak,[p] L. Shen,[o] Q. Wang,[g] E. Creegan,[c] S. Gaberšek,[h] I. Gultepe,[a,k] S. Hoch,[p] L. Lenain,[m] D. Richter,[a] R. Chang,[e] T. C. VandenBoer,[q] S. Bardoel,[a] A. Barve,[o] B. Blomquist,[i] T. Bullock,[f] Z. Chen,[q] L. Colosi,[m] R. S. Coppersmith,[a] I. Crawford,[n] L. R. Crilley,[q] R. Dimitrova,[a] A. Dowling,[a] D. Eleuterio,[j] S. Fiorino,[b] M. Gallagher,[n] N. Gapp,[l] G. Giacosa,[e] A. Grachev,[c] L. Grare,[m] T. Hintz,[a] C. Hocut,[c] K. Y. Huang,[a] O. Hyde,[a] K. Keefer,[b] D. G. Ortiz-Suslow,[g] A. Perelet,[p] W. Perrie,[d] J. Ruiz-Plancarte,[g] L. Salehpoor,[q] D. Singh,[p] N. Statom,[m] P. Taylor,[q] S. Wang,[a] and R. Yamaguchi[g]

KEYWORDS:
Fog;
Marine boundary layer;
Air-sea interaction;
Cloud microphysics;
Moisture/moisture budget;
Radiative forcing

ABSTRACT: Fog constitutes a thick, opaque blanket of air hugging Earth's surface, laden with small water droplets or ice crystals. Fog disrupts transportation, poses security threats, disorients human perception, and impacts communications and ecosystems. Collusion of atmospheric, terrestrial, and hydrologic processes produces fog droplets that pullulate over hygroscopic aerosols that act as condensation nuclei. Marine fog is particularly complex, since underlying dynamic, thermodynamic, and (bio)physicochemical processes span fifteen decades of spatial scales, from megameter-sized synoptic weather systems to nanometer-scale bioaerosols. This paper overviews the first international field campaign [Fog and Turbulence Interactions in the Marine Atmosphere-Grand Banks campaign (Fatima-GB)] of the project dubbed Fatima conducted during 1–31 July 2022 in the Grand Banks region of the North Atlantic. Therein, weather systems and commingling cold and warm oceanic waters provide entrée for fog genesis. Measurement platforms included an islet southwest of Nova Scotia (Sable Island), a research vessel (*Atlantic Condor*), an offshore oil platform, and autonomous surface vehicles. The instrument array comprised of extant remote and in situ sensors augmented by novel sensing systems prototyped and deployed in marine fog to penetrate the smallest scales of turbulence, examine aerosols, and quantify radiation budget. The comprehensive dataset so gathered, together with satellite and reanalysis products, mesoscale model, and large-eddy simulations, demonstrated that the long-held hypotheses of marine fog formation by warm air advection over colder water and in areas of enhanced (shelf) turbulence need to be revisited. The study also elicited new phenomena, for example, the fog shadow (clearings of fog downstream of islands).

DOI: 10.1175/BAMS-D-23-0050.1
Corresponding author: Harindra J. S. Fernando, fernando.10@nd.edu
Manuscript received 8 March 2023, in final form 30 January 2025, accepted 5 February 2025

SIGNIFICANCE STATEMENT: Fog research has escalated recently per climate change implications and directed energy (electromagnetic systems) applications. Here, we report selected findings of Fatima-GB, a comprehensive multidisciplinary field campaign conducted in Grand Banks, one of the world's foggiest areas, for improving the understanding and predictability of marine fog. Our findings indicate historical understanding of marine fog life cycle requires a fundamental rethink to incorporate complexities of scale interactions. Fog covers 15 decades of spatial scales, wherein megameter-scale synoptic systems sway millimeter-scale turbulent eddies, within which micron-scale fog droplets spawn on either tens (bioaerosols) or hundreds (sea salt) of nanometer-sized marine aerosols. We demonstrate the collusion of meteorological, oceanographic, turbulence, thermodynamic, and (bio)physicochemical processes during marine fog evolution, which should help develop future subgrid parameterizations for numerical weather prediction (NWP) models.

AFFILIATIONS: [a] University of Notre Dame, Notre Dame, Indiana; [b] Air Force Institute of Technology, Wright Patterson Air Force Base, Dayton, Ohio; [c] Army Research Laboratory, White Sands Missile Range, White Sands, New Mexico; [d] Bedford Institute of Oceanography, Dartmouth, Nova Scotia, Canada; [e] Dalhousie University, Halifax, Nova Scotia, Canada; [f] Digital Environment, WSP Canada Inc., St. John's, Newfoundland and Labrador, Canada; [g] Naval Postgraduate School, Monterey, California; [h] Naval Research Laboratory, Monterey, California; [i] NOAA/Physical Sciences Laboratory, Cooperative Institute for Research in Environmental Sciences, University of Colorado Boulder, Boulder, Colorado; [j] Office of Naval Research, Arlington, Virginia; [k] Ontario Technical University, Oshawa, Ontario, Canada; [l] Science Applications International Corporation, San Diego, California; [m] Scripps Institution of Oceanography and University of California, San Diego, San Diego, California; [n] The University of Manchester, Manchester, United Kingdom; [o] University of Minnesota, Minneapolis, Minnesota; [p] The University of Utah, Salt Lake City, Utah; [q] York University, Toronto, Ontario, Canada

1. Introduction

Fog is a collection of small airborne water droplets (size ~1–30 μm) that form near Earth's surface when an air mass becomes cooled and saturated, causing the horizontal near-surface visibility to drop below 1 km (Myers 1968; WMO 1992). Aerosols are essential for fog genesis, since they form the substrate [or fog condensation nuclei (FCN)] on which water vapor condenses to form droplets (Pruppacher and Klett 2010). The droplet growth is dependent on the (bio)physiochemical properties of atmospheric aerosols, meteorology, radiative forcing, and turbulence. Hygroscopic aerosols are considered "activated" when droplets reach a size conducive for further growth (Gerber 1981; Poku et al. 2019), while unactivated aerosols take up water and may remain airborne or settle through deposition processes (Farmer et al. 2021).

While the physical appearance of fog and clouds is nominally the same, profound dynamical differences exist between the two, due mainly to Earth's surface influence on fog. Fog occupies the lower atmospheric boundary layer (ABL), and processes therein undergird the *life cycle* of fog, namely, the formation, evolution/maturation, and dissipation (Nakanishi 2000). The vertical air velocities in the lower ABL are much smaller than the horizontal velocities, causing fog to be deprived of the main cooling mechanism that drives clouds: adiabatic expansion of ascending air (Rodhe 1962). Instead, fog relies on surface processes such as ground radiative cooling, moisture/heat fluxing, mixing of air masses, and surface

turbulence (MacDonald et al. 2020). Additionally, such local mechanisms are synoptically regulated, making fog a veritable multiscale phenomenon across a wide spatial continuum of fifteen decades—from global (10^7 m) to microphysical (aerosols, 10^{-8} m) scales.

Fog is broadly (and probably subjectively) classified into three categories: radiation, advection, and mixing fogs (Fernando et al. 2021). Nocturnal radiative cooling of a moist surface air layer leads to *radiative fog*. Advection of warmer air over colder water causes *advection fog*. Nonlinear mixing between nearly saturated warm and colder air masses produces *mixing fog* (Taylor 1917). Special categories are also common, for example, clouds of ice crystals near the surface (*ice fog*); fog droplets freezing on surfaces (*freezing fog*); steam streaks arising within colder fog (*steam fog*); rain evaporating into drier air (*precipitation fog*); and location-based fogs such as valley, upslope, and land fogs (Gultepe et al. 2016; Pu et al. 2023). Location fogs also include fog in the marine ABL (MABL), *marine fog*—a type of extreme complexity and among the least predictable in meteorology.

Contributing to the intricacy of marine fog are a myriad of upper-ocean, air–sea interaction, and MABL processes illustrated in Fig. 1. Additional phenomena may appear at the transition between ocean and land (coastal zone). Koračin et al. (2014) and Koračin and Dorman

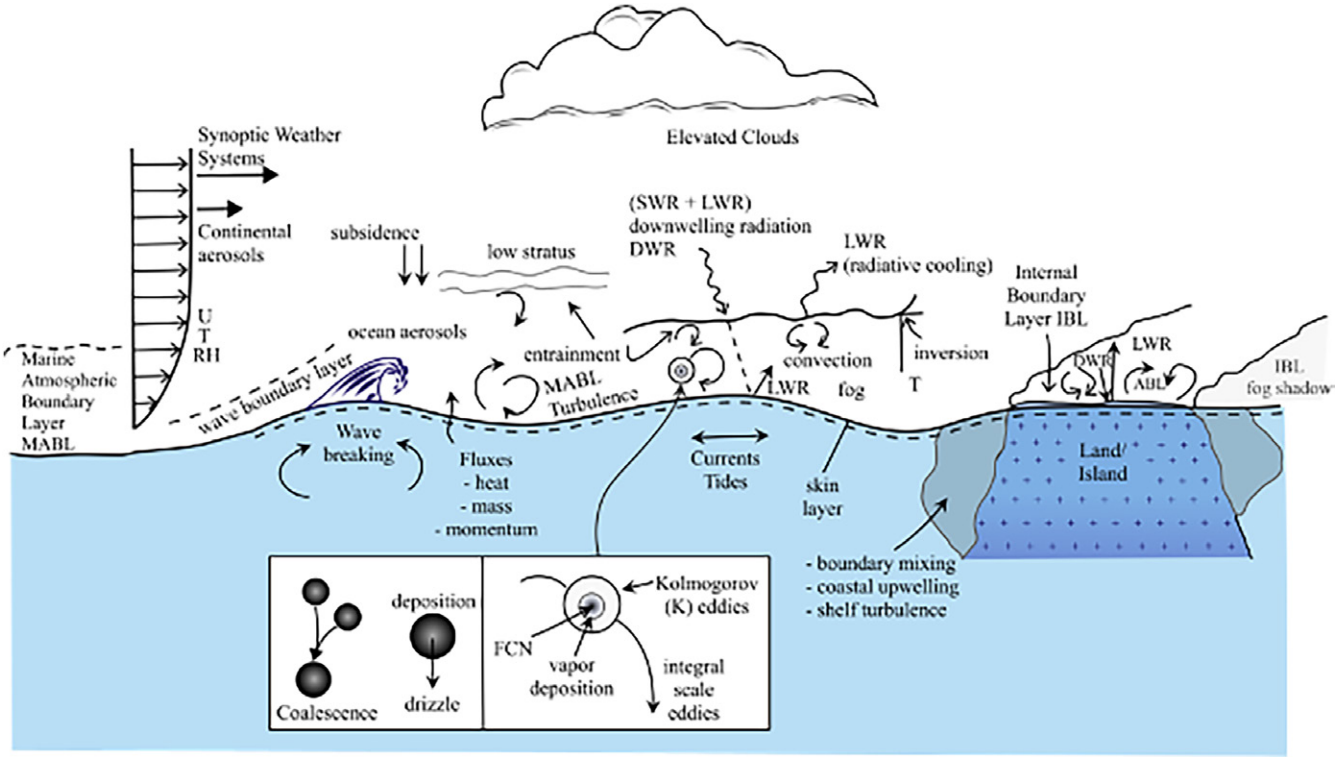

Fig. 1. Marine fog processes—advected continental or marine hygroscopic aerosols act as FCNs. Water droplets grow around FCNs by diffusional deposition of vapor (inset). Köhler (1936) argued that droplet growth requires exceeding a critical radius determined by opposing effects of surface tension and solute concentration (whence droplet vapor pressure increases/decreases, respectively). The role of the smallest turbulent (K) eddies in the ABL, within which FCNs are imbedded, however, is yet to be understood (inset). Note that, for the air, K scales and O–C temperature dissipation scales are of the same order, and hence, the temperature within the K eddies or immediately surrounding FCNs is homogeneous. Spawning droplets undergo coalescence and settling (inset). Contributing upper-ocean processes/phenomena include waves and breaking, nocturnal convection, turbulence and mixing, tides, and currents. The corresponding lower-atmospheric phenomena include wave boundary layer and shear and convective turbulence. At the air–sea interface, turbulent heat, mass, momentum, and aerosol exchanges occur by wave breaking and surface renewal via the (molecular) skin layer, which fuel air–sea interactions. SWR/LWR and advective processes also affect SST. Vital contributions of MABL come from synoptic and mesoscale (advective) systems including fronts, highs and lows, inversions, heating/cooling of the sea surface and fog top, diel cycle, clouds, turbulence, and aerosols. If present, coastal contributions from boundary mixing, upwelling, escalated wave breaking, land/ocean (differential) heating, and IBLs have significant impacts on fog life cycle.

(2017) provided extensive reviews of marine fog. Coastal fog has been studied extensively, e.g., along the U.S. West (Leipper 1994) and East (Fernando et al. 2021) Coasts and elsewhere (Spirig et al. 2019). Both *sea fog*, marine fog in the shallower "green" water away from the coastal zone, and *open-ocean fog* over the deeper "blue" water remain under-researched. The megaproject described in this article, dubbed fog and turbulence interactions in the marine atmosphere (Fatima), shifts attention to these understudied deeper waters and explores new frontiers of knowledge on sea fog; see appendix A. For general acronyms, see appendix L.

Low visibility in fog disrupts all modes of transportation, critical industrial operations such as oil platforms, and free-space optical communications (Gultepe et al. 2009). The hazardous human health impacts of chemically active, pollutant-trapped, *smoky fog* (smog and thicker super fogs, visibility <3.3 m) have been well documented (NWS 2024). Coastal fog has profound ecological consequences (Torregrosa et al. 2014). Marine fog is considered as an "unknown" in asymmetric warfare, for example, when a swarm of small boats or unmanned aerial system (UAVs) are the blurred threat, whence, for defense, directed energy systems such as high energy lasers (HEL) and optically guided weapons are tools of choice (Pawlak 2012; Niece and Kaiser 2018). The shorter the wavelength, the higher the intensity of lasers on the target (Jumper and Gordeyev 2017), and thus, HEL applications prefer near-IR and visible wavelengths; such beams are stymied by the presence of fog (Perram et al. 2010). Fog is also evaluated as a potable water source amid dwindling water supplies due to climate change (Bhushan 2020).

Understanding the nexus between fog, aerosols, radiation, flow, and turbulence is critical for the prediction of fog life cycle. Notwithstanding, owing to a lack of high-resolution data and solid theoretical bases, numerical weather prediction (NWP) models employ parameterizations based on cloud research for fog prediction and unsurprisingly struggle for accuracy (Gultepe et al. 2006; Van der Velde et al. 2010; Boutle et al. 2018). Modeling studies typically invoke similarities between stratocumulus clouds and fog (Karimi 2020). Thus, melding of knowledge from multiple disciplines—meteorology (ABL and free atmospheric flow), fluid mechanics (advection, turbulence, and instabilities), thermodynamics (heat transfer), microphysics (aerosols and droplets), and (bio)geochemistry (gas–aerosol production, interactions, and transformations)—is imperative for improvements in fog prediction, which was the approach used in Fatima.

Fatima focused on two geographical areas of highest summer marine fog occurrences in the world. Based on climatology maps, Dorman et al. (2017) identified 16 fog maxima over shallower water during the warm season. The two most prevalent (excluding antiaccess/area-denial) sites were the southeast of the Grand Banks off Newfoundland (~50–200-m water depth) with a peak fog occurrence of 45% during June–August (JJA) and the Yellow Sea with 18% fog occurrence (~10–80-m depth, JJA); both belong to the sea fog category. Field campaigns at both sites have been completed, with the Grand Banks campaign (Fatima-GB) during 1–31 July 2022 and Fatima-YS during 20 June–8 July 2023. Given different basins and geographic and synoptic settings, stark disparities between fog–genesis mechanisms (e.g., oceanic versus continental aerosols) were expected from the two sites.

Given the intrinsic merits of each campaign, this article exclusively concerns Fatima-GB. Dorman et al. (2017, 2020) hypothesized that southerly/southwesterly airflow over the negative northward sea surface temperature (SST) gradients in Grand Banks, caused by mingling between Gulf Stream and Labrador waters, is an important contributor to sea fog therein (appendix A). Contrary to the common belief that fog correlates with low ABL turbulence, the fog maximum in Grand Banks occurs at relatively higher median wind speeds (Isaac et al. 2020) and elevated turbulence levels associated with cyclonic systems passing over toward the North Atlantic. This article summarizes the execution and a few representative results of Fatima-GB, simultaneously covering synoptic to microscales—a pioneering study of its kind. Continuing challenges to sea fog research are also discussed.

2. Design and execution of Fatima-GB

Capturing larger-scale weather systems down to Kolmogorov (K) scales (Van der Hoven 1957) and investigating regions of enhanced oceanic turbulence apropos of Grand Banks summer fog were the principal design considerations. The selected geographic area of the campaign and the Canadian Research Vessel, *Atlantic Condor* (R/V *Condor*), that traversed the domain are discussed in appendix B. The principal measurement locations were the (i) Grand Banks, a region with complex topography on the North American continental shelf; and (ii) Sable Island, an isolated, Canadian-owned, croissant-shaped sandbar well exposed to the advection path of fog. Both R/V *Condor* (Fig. 2) and Sable Island (Fig. 3; appendix C) were densely instrumented for capturing synoptic to mesoscale weather and ABL parameters such as turbulence and fluxes, turbulent kinetic energy (TKE) and temperature-fluctuation dissipations at K and Obukhov–Corrsin (O–C) scales (at Sable), radiation, water vapor and hydrometeors, visibility, electro-optic and electromagnetic (at Sable) propagation, (bio)physicochemical properties of aerosols, SST, hydrophysical and turbulence properties of upper ocean, and surface waves. Continuous meteorological and visibility data from cooperating offshore installations (e.g., Hibernia Oil Platform) were also available. Instruments are listed below and further elaborated in appendix K with acronyms. For research group acronyms, see appendix A.

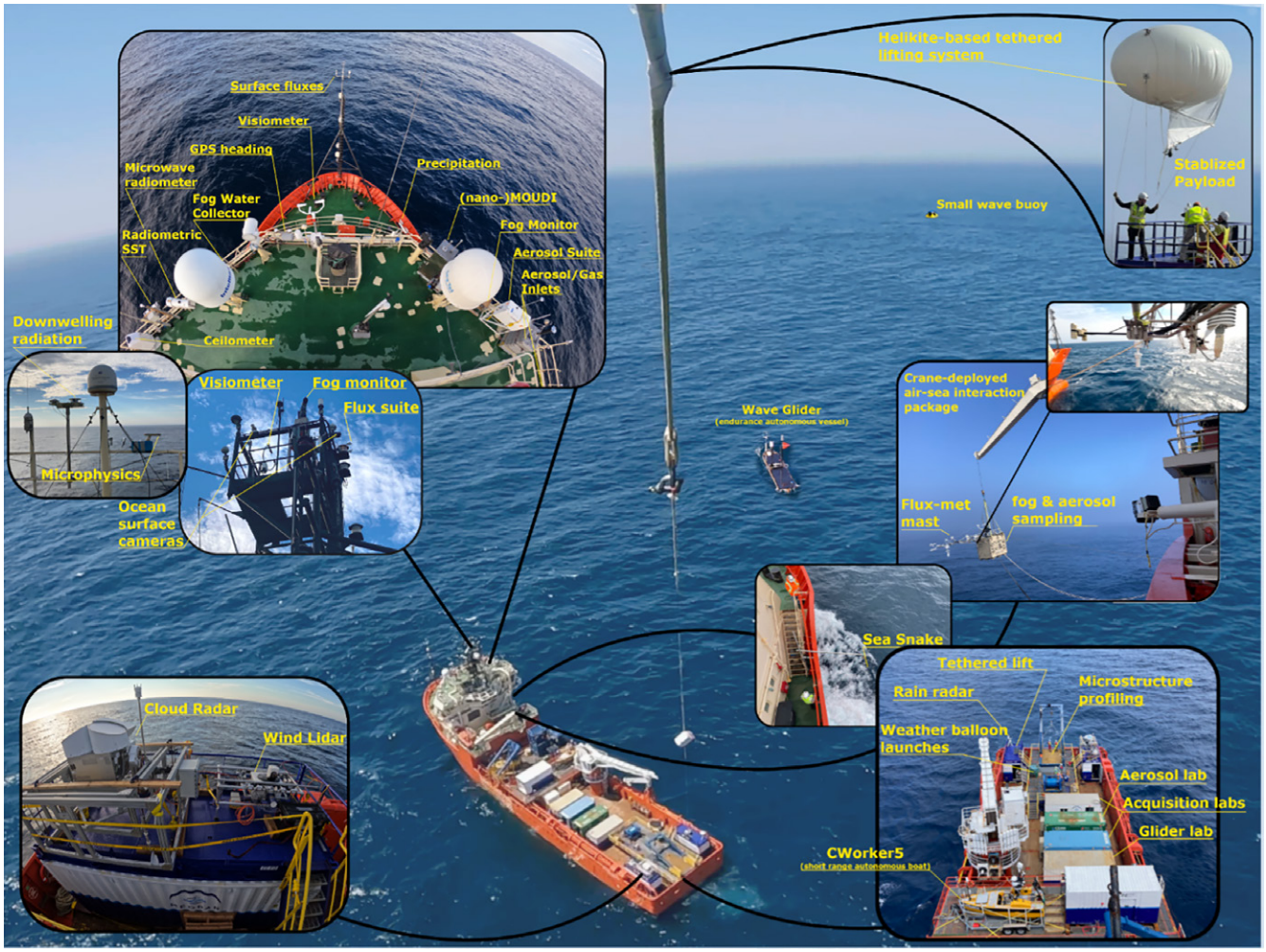

Fig. 2. Instrumentation on R/V *Condor*. This deep-sea supply vessel was converted to a research vessel by the Fatima group after extensive retrofitting. R/V *Condor* was on lease from Atlantic Towing Ltd. through the Marine Environmental Observation, Prediction and Response (MEOPAR), a Canadian National Network of Centers of Excellence on marine research. It was made available at a time when U.S. vessels were unavailable due to COVID-19-related postponements/queuing.

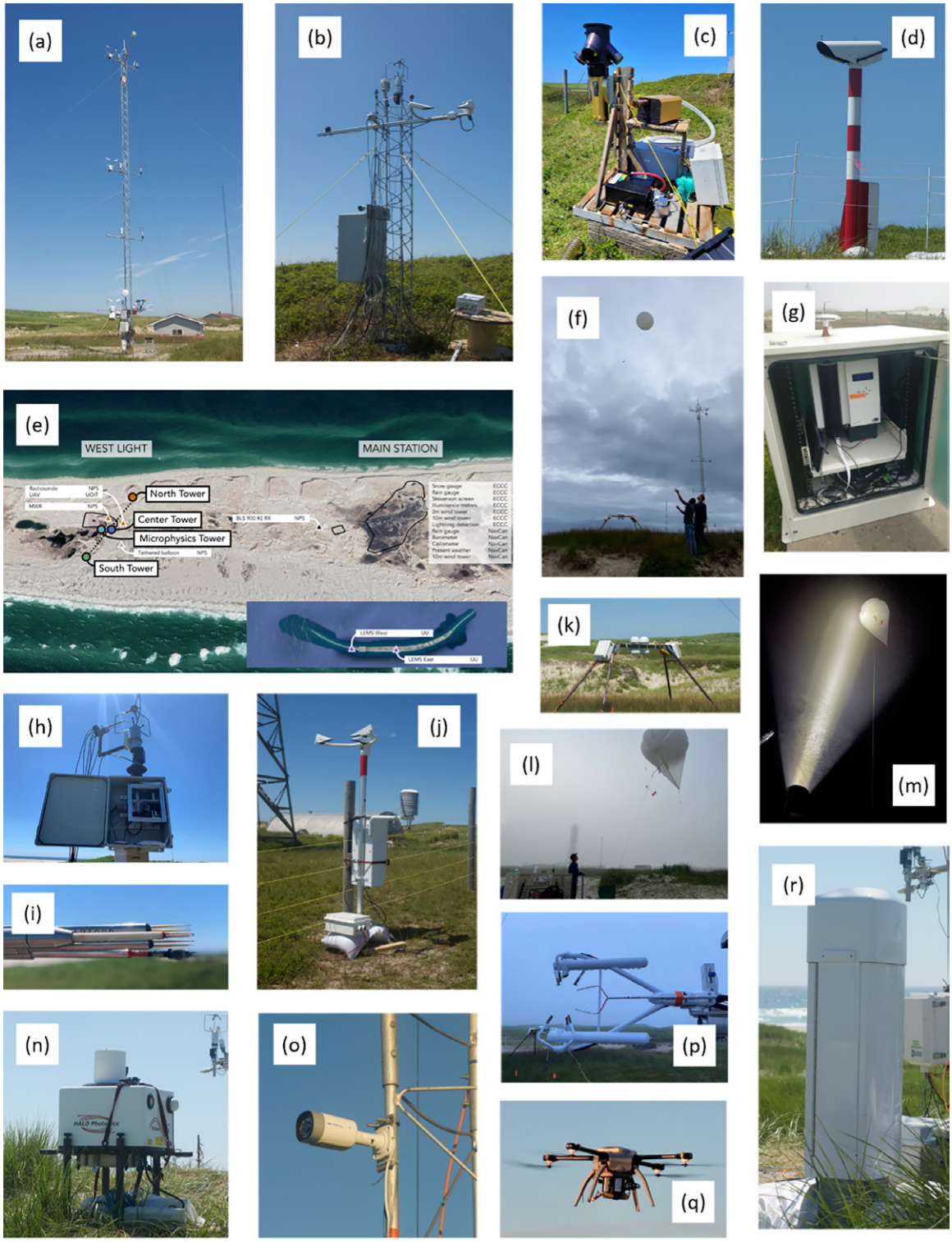

Fig. 3. A sample of instruments at Sable. (a) The central flux tower; (b) the microphysics tower; (c) FM120 and GCIP; (d) transmissometer (LT31); (e) map showing the tower transect and two satellite sites; (f) rawinsonde releases; (g) CINCS; (h) Super Combo system for TKE and *T* dissipation measurements; (i) Super Combo probe ensemble; (j) FD70; (k) radiation balance measurements on sawhorse structure; (l) TLS profiling system; (m) TLS profiling with fog/mist visualization using a powerful flashlight; (n) Halo Photonics Doppler wind lidar; (o) webcam; (p) LWC probe within an IRGASON probe volume; (q) UAV with meteorological instruments; (r) Vaisala CL31 ceilometer. Instruments on each tower are also in appendix C.

a. Instrumentation on R/V Condor (Fig. 2).

1) Instruments.

University of Notre Dame (UND): microwave rain radar (MRR-PRO), microwave radiometer (MWR), uprising vertical microstructure profiler (VMP-250), optical disdrometer, CTD, 300-kHz ADCP, sea snake, visible and cloud/IR cameras, remote ocean sensing radiometer (ROSR), FD70 visibility sensor, ceilometer CL61.

Naval Postgraduate School (NPS): small moored wave buoy, rawinsondes, surface and scene visualization cameras.

University of Utah (UU): pyrgeometer and optical particle counter (OPC-N3) for tethered lifting system (TLS).

Dalhousie University (DU): fog water collector, scanning mobility particle sizer (SMPS), aerodynamic particle sizer (APS), fog monitor FM120.

York University (YorkU): micro-orifice uniform deposit impactor (MOUDI), nano-MOUDI-II, ion chromatograph, gas monitors.

Air Force Institute of Technology (AFIT)/NPS: integrating nephelometer, black carbon aethalometer, condensation particle counter (CPC).

2) Instrument Systems.

UND: Doppler lidar and W-band (cloud) radar, both on motion-stabilized platforms.

Physical Sciences Laboratory at NOAA (PSL-NOAA)/UND: bowmast (3D Sonic, LI-COR 7500, weather transmitter (TX) WXT520, GPS, pressure (HMP), pyrgeometer, pyranometer).

UU/Army Research Laboratory (ARL)/UND: TLS with meteorological and turbulence packages. Gimbaled pyrgeometer.

NPS: Crane-Based Cloud and Aerosol Measurement System [C-CAMS; an in-house developed fog/aerosol/turbulence sampling system measuring carbon dioxide (CO_2) and water vapor fluctuations [integrated open-path gas analyzer and sonic anemometer (IRGASON)], platform motion [VectorNav 300 (VN-300)], pressure fluctuations (MET4A), radiometric SST (CT-15), relative humidity (RH) and temperature (T) (HMP155), visibility and meteorology [Campbell Scientific (CS-125)], upwelling radiation (infrared pyranometer), net radiation, surface elevation (radar altimeter), aerosol absorption (soot photometer), aerosol size spectra [portable optical particle spectrometer (POPS)], fog droplet parameters (FM120)], deck-mounted CAMS (D-CAMS).

Ontario Technical University (OntTechU): backscatter cloud probe (BCP) and cloud droplet probe (CDP-2) on the Gondola Platform.

Scripps/University of California, San Diego (UCSD): instrumented wave gliders [3D Sonic, WXT530, CTD, profiling CTD, 300-KHz ADCP, current profiler, dual-GPS receiver (RX), GPS-aided inertial measurement unit (GPS-IMU)] and uncrewed surface vessel (A/V Wallace, L3Harris C-Worker 5 with 2xSonics on a flux mast, FM120, towed CTD, 500-Hz ADCP, visible and IR 360 cameras, X-band radar).

b. Sable (Island) campaign (Fig. 3). Sable has an average width of ~700 m (1.2 km at its widest point) and a length of ~40 km and is characterized by relatively simple topography with a maximum elevation of 30 m, minimal geographic changes from ocean to land, and low (~1-m height) grass coverage without vegetation. Being devoid of human footprint (i.e., anthropogenic heat and factitious elements that may alter fog thermodynamics), Sable is an ideal location to study marine fog and land interactions. Operated by the Parks Canada Agency as a strict nature reserve, it is a migratory bird sanctuary for over 2500 pairs each

of terns and gulls nesting and breeding in the summer. During Fatima-GB, Sable was the homestead for 569 feral horses, with beaches roamed by a colony of harbor and gray seals.

Appendix C shows a plan view of Sable Island, along with two main deployment areas (Main Station and West Light), instruments, and their owners. The Main Station was operated remotely, without disturbing tern nests that may eschew bird strikes. The backbone of West Light was an array of three (north, center, and south) towers along the climatologically streamwise (southwest–northeast) transect, with instrument clusters surrounding them. Parks Canada required strict compliance with Canadian ecological conservation ordinances, accompanied by permits. Accordingly, instrument clusters were located in Parks-approved areas of little to no protected vegetation within electric-fenced enclosures to safeguard both horses and equipment. Food and power are not available at Sable, and Parks-provided gas-powered generators were the electricity source. Routine charter aircraft services (and occasional helicopters in bad weather) were the reliable transportation link between mainland and Sable. An eight-member research team occupied an existing house in the West Light, with supplies flown in from Halifax. According to Parks Canada, Fatima-GB was the first large-scale meteorological field study ever conducted at Sable. The instrumentation listed below including acronyms is further detailed in appendix K.

1) Instruments.

UND: FD70, present weather detection-22 (PWD22) visibility sensors, scanning Doppler lidar, net radiometers, LI-COR, Sonics, fine-wire T/RH sensors, ceilometer CL31.
NPS: MWR, sodar, scintillometer, differential image motion monitor, wide-angle (teleradiometric) transmissometer, noncoherent extended source beacon, rawinsondes, TLS, CS120 visibility sensor, CDP, transmissometer, differential temperature sensors (DTSs), IRGASON, video cameras.
UU: MRR-PRO, ceilometer CL31, infrared electromagnetic propagation system (scintillometer BLS900), microwave scintillometer (RPG-MWSC-160), OPC-N3, visibility cameras, liquid water content (LWC) probes, soil heat flux sensor, soil moisture and temperature *T* sensor (CS650), soil *T* probe, CS125.
AFIT: Cloud ice nucleation characterization system (CINCS).
University of Manchester (UMAN): multiparameter bioaerosol spectrometer (MBS).

2) Instrumented Systems.

UND: Super Combo probe (in-house built) to capture *T* and scalar dissipation in turbulence.
NPS/UU: TLS with temperature, RH, wind speed/wind direction (WD), pressure, OPC-N3, pyrgeometer.
UU/UND: flux towers.
UU: local energy budget measurement system (LEMS) automated weather system; precision radiation balance sawhorse [four components of shortwave (SW), longwave (LW), and net radiation].
OntTechU: UAV (with *T*, P, RH, OPC-N3 probes), microphysics supersite [ceilometer CL51, WXT520, PWD52, FM120, ground cloud imaging probe (GCIP), 3D Sonic, sunshine pyranometer, digital camera for local view].

Limited surface weather, visibility, and microphysics data (from PWD50, FM120, WXT520, CL31) at 1 min, mixed with 15-min and 1-h data, were provided by the Hibernia site during June–August 2022.

3. IOPs and ISPs

Although most instruments operated continuously, expensive, labor-intensive, and high-maintenance systems such as high-frequency rawinsonde launches (8–24 per day instead of 4 per day), VMP-250, and C-CAMS were operated only during intense operational periods (IOPs). In general, IOPs were called during (virtual) weather briefings conducted daily at 1300 Atlantic Daylight Time (ADT) by a group of ~13–20 participants. For guidance, NRL used the Coupled Ocean–Atmosphere Mesoscale Prediction System (COAMPS)[1] operational mesoscale model at 1-km resolution with initializations at 48, 24, and 12 h ahead (Hodur 1997). YorkU used the WRF Model (Skamarock et al. 2008) with 10-km resolution, generating simulations from 1800 to 1800 UTC next day after a spinup time of 12 h. Both models used the Global Forecast System (GFS) model for initial and boundary conditions and generated hourly forecasts. Horizontal maps and vertical profiles at selected locations were examined. Also used were GFS (resolution 0.25°) output, GOES satellite imagery, weather radar, radiosonde observation (RAOB), and NOAA HYSPLIT backtrajectories (UCSD and OntTechU). For Sable, an IOP was invoked by group consensus when conditions for capturing at least parts of the fog life cycle appeared favorable. IOPs typically lasted 24–36 h, except for propitious 72-h "super-IOPs." Table 1 lists the IOPs. Fog (visibility <1 km) appeared during 9 of the 14 IOPs.

[1] COAMPS is a registered trademark of the U.S. Naval Research Laboratory.

Naturally, IOPs for Sable Island were not optimal for R/V *Condor*, which trekked in and out of fog (Figs. 4a–c). As such, suitable study periods, dubbed intense study periods (ISPs), were identified *posteriori* using the following criteria beneficial for later analysis: (i) visibility < 1 km, (ii) relative wind direction within ±60° of the bow course, and (iii) ship speed <3 m s^{-1} (and winds generally >5 m s^{-1}). Figure 4 shows the visibility, rawinsonde, meteorological, and microphysical information for five ISP periods identified using the above criteria. A list of ISPs is shown in Table 2.

Table 1. IOPs for SI (ADT = UTC – 3 h). J = July. BR, FG, DRZ, and RN signify mist, fog, drizzle, and rain conditions, respectively. HP, LP, CG, MX, and ST refer to the high pressure, low pressure, convergence zone, mixing, and stable synoptic conditions, respectively. Local conditions may change over the course of IOPs. Note that FG, BR, and DRZ transitions (identified by FD70) are not very smooth and may be lumped all together.

IOP No.	Start (ADT)	End (ADT)	Hydrometeor type (PWD22/FD70)	UAV	TBS	Rawinsonde frequency	Observer notes	Synoptic setup
1	J03_1800	J04_1800	FG/BR/DRZ/RN	√	x	√ (3 h)	Mix hydrometeors	HP/MX
2	J06_1800	J07_1800	DRZ/RN	√	x	√ (3 h)	Rain/mist	CG/MX
3	J09_2100	J11_0130	BR/patchy fog	√	√	√ (3 h)	IOP-wavy structures	LP/ST
4	J12_1800	J13_1500	CLR	x	√	√ (3 h)	Failed fog/reference case/visibility fluctuations	LP/ST
5	J13_1800	J15_1500	BR/CLR	x	√	√ (3 h)	Super-IOP, excellent FG event	HP/MX
6	J15_1500	J16_0900	FG/BR/DRZ/RN	x	x	√ (3 h)	FG but windy	HP/ST
7	J17_1800	J18_1800	FG/BR/DRZ/RN	x	√	√ (3 h)	FG front, extended IOP	HP/ST
8	J18_1800	J20_0900	FG/BR/DRZ/RN	x	x	√ (3 h)	FG and high wind	HP/ST
9	J21_1500	J22_1500	FG/BR	x	√	√ (3 h)	Excellent FG formation/persistent	HP/ST
10	J23_1200	J25_1800	FG/BR/DRZ/RN	x	√	√ (3 h)	Super-IOP, Advection FG; strong winds; FG shadow predicted	HP/ST
11	J26_0600	J27_0600	BR	x	x	√ (1 h)	Late FG shadow possible, dissipates early morning	CG/MX
12	J28_2100	J28_2330	FG/BR/DRZ/RN	x	√	√ (12 h)	Thin barely visible FG layer/BR, radiation impact, light drizzle	CG/ST
13	J29_1600	J30_1800	BR/RN	x	√	√ (3 h)	Postfrontal FG/stratus lowering/light rain after fog	LP/MX
14	J30_1800	J31_0900	FG/BR/RN	x	x	√ (3 h)	Rain and 1.5-h FG on next morning	LP/MX

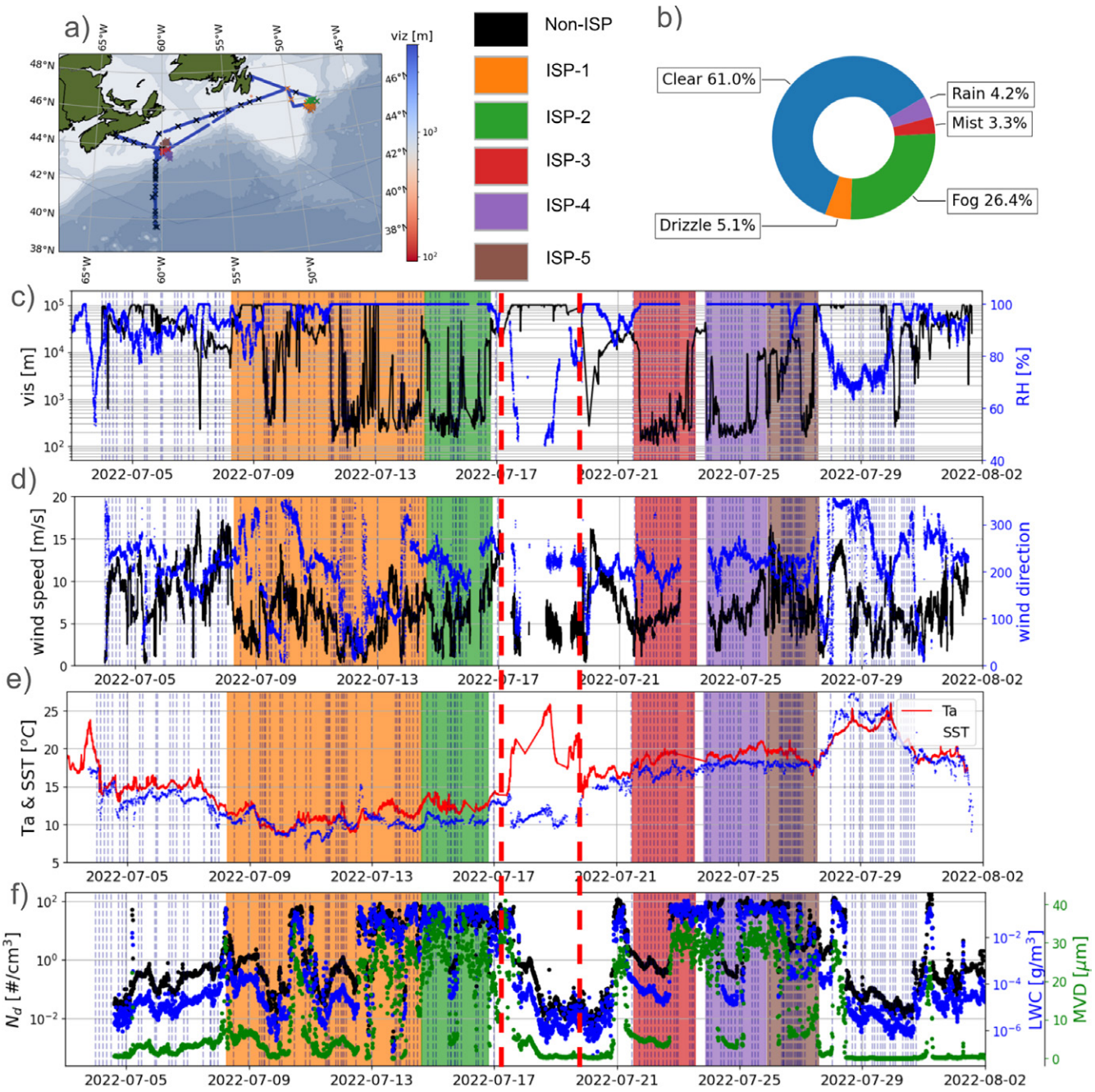

Fig. 4. (a) Condor track with rawinsonde release locations (x), color at each location indicating visibility (from FD70); (b) pie chart of hydrometeor status (FD70) during the campaign; (c) visibility (FD70) and ISP durations identified in color shading based on the criteria in the text (also see Table 2); (d) ambient WS WD (bowmast); (e) air *T* and SST (bowmast and ROSR); (f) aerosol number concentration N_d, LWC (FM120), and MVD. Red vertical broken lines demarcate the port call of R/V *Condor* at St. Johns, Newfoundland. The vertical dashed lines indicate the times of radiosonde launches, corresponding to (a).

Table 2. ISPs at R/V *Atlantic Condor*.

ISP	No. of rawinsondes	Start time	End time	Comments
1	32	0610 UTC 8 Jul	1450 UTC 14 Jul	Significant synoptic systems passing through (at the shelf break; near Hibernia)
2	13	1510 UTC 13 Jul	1900 UTC 16 Jul	Approximately constant WD (at the shelf break; near Hibernia)
3	15	1240 UTC 21 Jul	1300 UTC 23 Jul	Near SI on the shelf
4	13	2100 UTC 23 Jul	2030 UTC 25 Jul	-ditto-
5	19	2130 UTC 25 Jul	1330 UTC 27 Jul	SLOP

4. Data repository

The primary means of data storage is Google Drive, allowing quick and convenient access and secure cloud storage. At present, data from individual groups have been saved into a shared Google Drive. A mirrored hard drive is also maintained. Types of data being uploaded include raw data, processed intermediate data, and quality-controlled data for improved accountability in data analysis. Supporting datasets such as satellite imageries and model forecast/reanalysis used by the forecasting group are also cataloged and saved. All datasets will be available for the science community after 1 August 2025.

5. General observations

In addition to those of R/V *Condor* shown in Fig. 4, representative observations at or near Sable Island are shown in Fig. 5 as time series of meteorological, thermodynamic, turbulence, microphysical, and surface variables from the central tower, a total of 182 soundings, and by the wave glider "Carson" operating in the shallow waters southwest of Sable that provided nominal upwind upper-ocean and lower-atmospheric conditions. Shaded periods in Figs. 5a–o are IOPs. Note the (i) predominant southerly/southwesterly wind direction (Fig. 5a); (ii) wind perturbations in response to diurnal temperature cycle at low wind speeds (Fig. 5a); (iii) weak diurnal variability of SST and marine T_{air} (Fig. 5l); (iv) elevated LWC, mean volume diameter (MVD), and N_d during IOPs with fog, consistent with previous measurements (Gultepe et al. 2021) in marine fog in the North Atlantic (Figs. 5g–i); (v) (predominant southwesterly/westerly) winds punctuated by occasional periods of heightened wind speeds aloft up to 20 m s^{-1} (Fig. 5p); and (vi) persistently moist air (RH > 80%) with propensity for saturation that frequently extends beyond 1.5 km (Fig. 5r). Extensive campaign-wide data of the ilk illustrated in Figs. 4 and 5 have motivated a variety of ongoing process and numerical studies.

The daily averaged aerosol number concentration on the R/V *Condor* is shown in Fig. 6a for both fog and no-fog conditions. During 4–17 July, the R/V *Condor* was in Grand Banks away from Sable Island (dubbed Grand Banks Period), whereas it was in the vicinity of Sable Island during 19 July–1 August (Sable Period). A larger aerosol concentration occurred in coastal areas close to Nova Scotia (during 3–4 and 30–31 July), around Sable (21–25 July), and toward the Gulf Stream (27–29 July). Lower aerosol concentrations were observed in Grand Banks (10–13 July), suggesting less continentally influenced air, consistent with the CO measurements shown in Fig. 6b. In contrast, a higher aerosol concentration occurred in coastal areas close to Nova Scotia during 3–4 and 30–31 July, around Sable (21–25 July), and toward the Gulf Stream (27–29 July), suggesting more pollution influence, also consistent with the CO measurements (Fig. 6b).

Overall, <100-nm aerosols accounted for ~60% and 100–200 nm for ~30% of the total number concentration (appendix D), demonstrating the controlling influence of smaller particles. During fog, the median particle number concentration decreased by 40% and 30% for particles in the ranges of 10–100 and 100–200 nm, respectively, but did not show significant change for the larger particles. It appears that smaller particles were more susceptible to losses due to Brownian diffusion leading to wet scavenging, as observed in clouds (Greenfield 1957). Conversely, particles >200 nm were unaffected by fog, causing an increase in their relative contribution (Wu et al. 2022).

In matters of gridded gas mixing-ratio observations (Fig. 6b), being further from major anthropogenic emission regions, the Grand Banks period is less burdened with the combustion tracer CO compared to the heavily trafficked Sable period (75 vs 140 ppbv), the latter being closer to the dominant continental outflow of the North American seaboard. Similarly, enhanced ozone (O_3) was present in the Sable region (40 vs 30 ppbv for Grand Banks). Observations of NO_x and total reactive nitrogen tN_r were similar in both locations, indicative of NO_x being the primary component of tN_r. Secondary photochemical species (e.g., O_3) are indicative

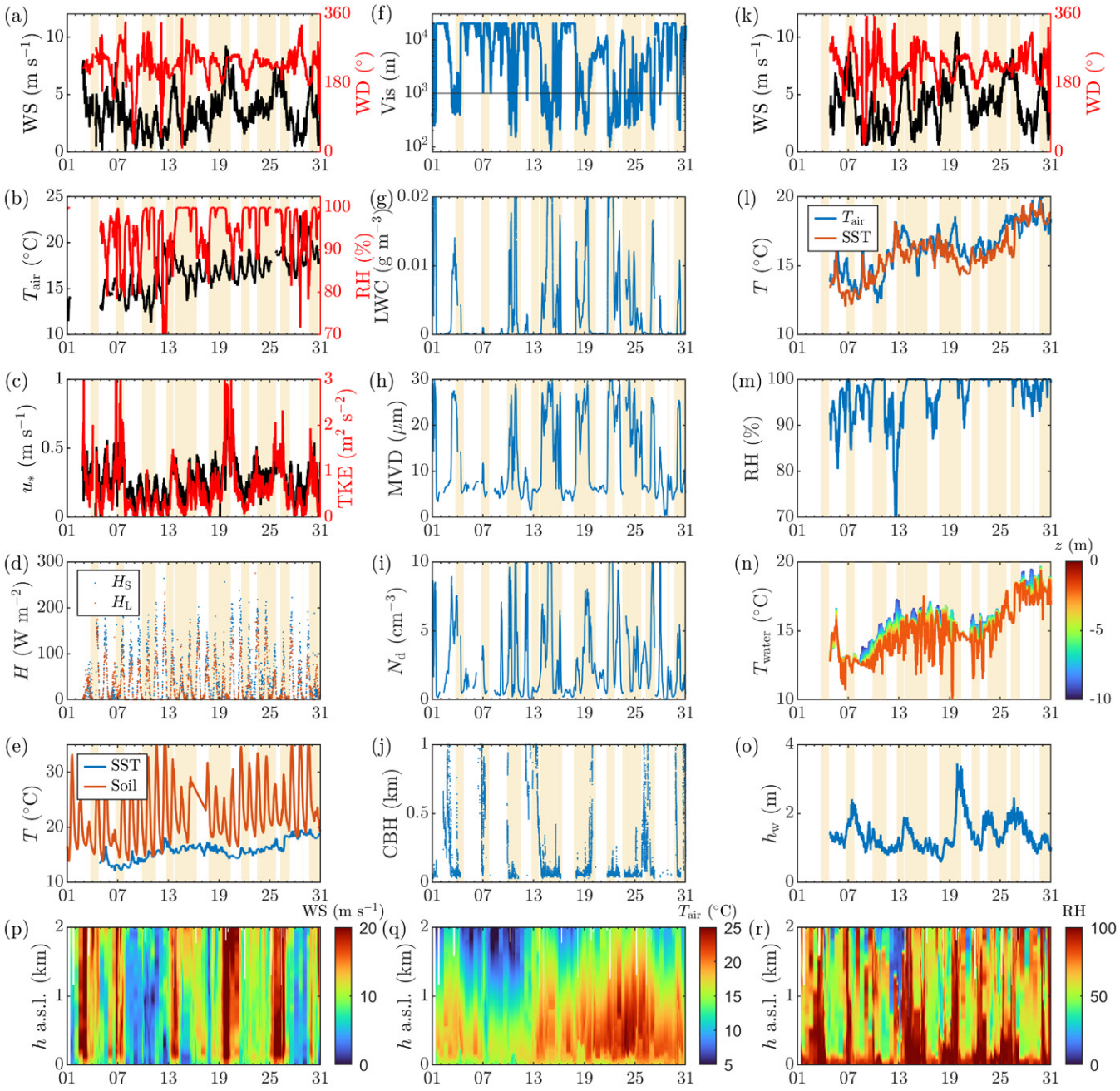

FIG. 5. Data from the (a)–(e) center tower (15 m), (f)–(j) microphysics station, (k)–(o) wave glider Carson operating 30–60 km southwest of Sable (Grare et al. 2021), and (p)–(r) radiosondes (3–4 per hour). (a) 2-m WS and WD; (b) 2-m air temperature T_{air} and RH; (c) 2-m friction velocity u_* and TKE; (d) 2-m sensible and latent heat fluxes H_s and H_L; (e) soil temperature T_s and SST; (f) visibility Vis (1-km threshold or fog is identified by a horizontal line); (g) LWC; (h) MVD; (i) droplet number density N_d; (j) cloud-base height (CBH); (k) WS and WD [(k)–(o), from wave glider Carson]; (l) T_{air} and SST; (m) RH; (n) water temperature T_{water}; (o) significant wave height h_w; (p) WS [(p)–(r), from rawinsondes]; (q) T_{air}; and (r) RH. For instrument details, see appendix K.

of the pollution regime (Lakra and Avishek 2022), and novel chemical measurements such as tN_r accomplished in Fatima-GB enable the study of particle and droplet composition thermodynamics of fog.

6. Archetypal process and case studies

a. Synoptic weather systems—A trigger for fog. Synoptic analyses during Fatima-GB suggest that the (longstanding) hypothesis—northward advection of air masses over the Gulf Stream causes them to be warm and humid, which, when passing aloft colder Labrador water, creates conditions for escalated summer fog in Atlantic Canada (appendix A)—is

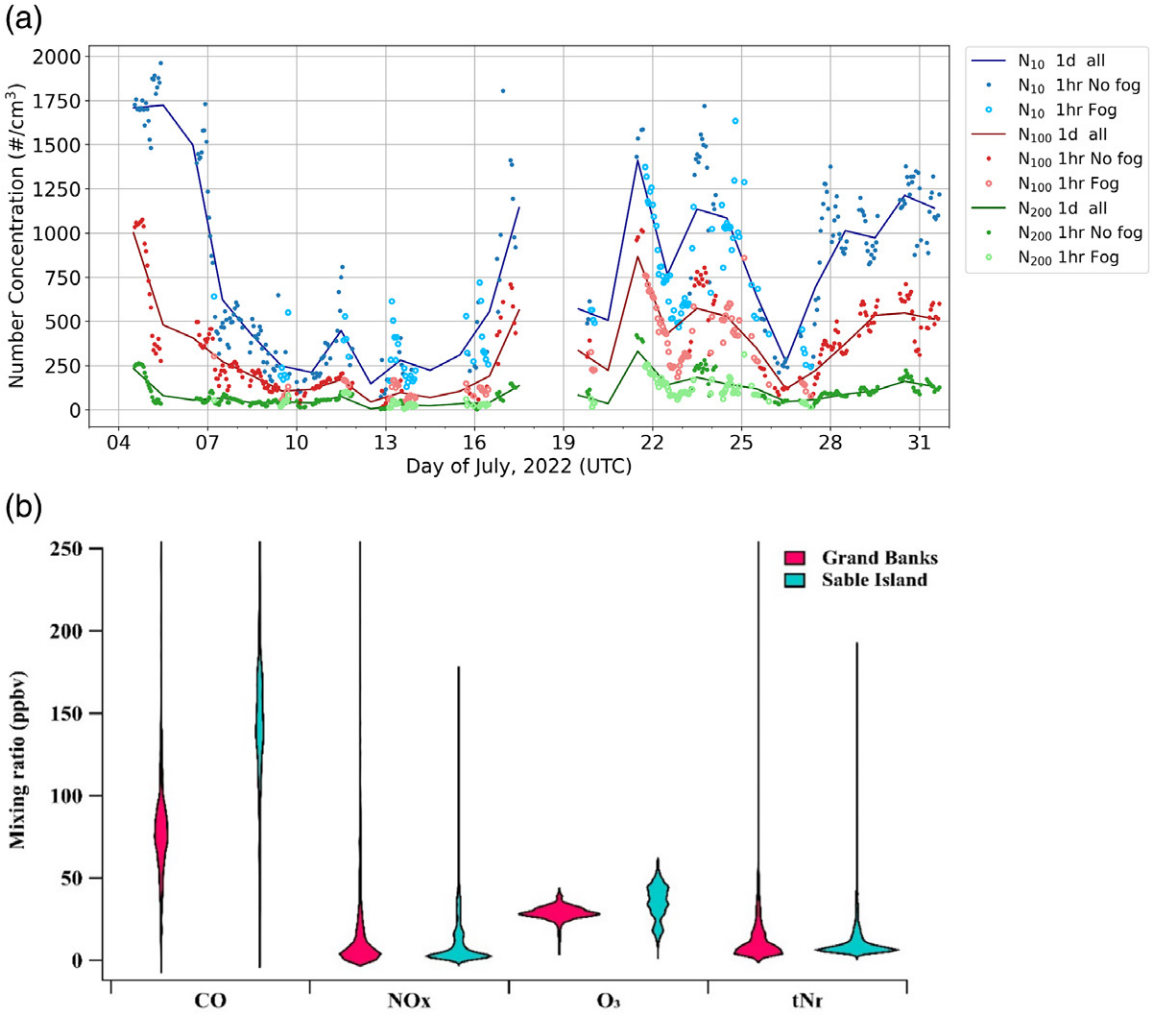

FIG. 6. (a) Aerosol number concentration from 10.6 to 496 nm measured with the SMPS on the ship bridge (appendix K). N10 (blue), N100 (red), and N200 (green) indicate the number concentrations of all aerosols with diameters >10, 100, and 200 nm, respectively. The solid lines represent daily (1d) averages, small dark solid circles are hourly (h) averages during no fog, and large bright circles are hourly averages during fog. The aerosol inlet sampled dry aerosols at 19 m MSL and traveled through 11.35 m of stainless-steel tubing before being measured by the SMPS. The gap of observations during 17–19 Jul was due to the port call. (b) A violin plot of atmospheric pollutant distributions of combustion product mixing ratios that are long lived like carbon monoxide (CO) or moderately lived like nitrogen oxides ($NO + NO_2 = NO_x$). The NO_x was analyzed via chemiluminescence (Ecotech EC9841), ozone via non-dispersive ultraviolet absorption (Ecotech S10), and CO via infrared absorption spectroscopy (Ecotech EC9830). The instruments were on the ship bridge and sampled outdoor air from a common sampling manifold passing through the ceiling to the deck above the pilothouse and positioned the bow side (upwind) of the ship exhaust. A custom-built instrument for measuring total gaseous reactive nitrogen (tN_r) and its basic fraction [e.g., species like ammonia (NH_3) and amines (NR_3)] were also sampled from the manifold (Crilley et al. 2023).

untenable. The bulk of the July 2022 surface winds at Sable was southwesterly, following the northward advection path, but fog occurred at Sable only 30% of the time. Fog genesis mostly required a synoptic trigger, a prospect being eastward-propagating deep lows across eastern Canada. Such systems have broad southward-oriented troughs that extend across the Atlantic coast and beyond Sable, almost always accompanied by a broad cloud band with low overcast ceilings (~60 m) and lowered visibility (~1–3 km). After the leading edge passes over Sable, there are occasional fog periods, and a trailing ridge encroaching into the middle and lower layers lowers the cloud top and ultimately terminates fog and clouds.

An example is the IOP1, with a cloud band lowering over Sable at 0200 UTC 3 July and dropping visibility below 4.8 km and ceiling below 915 m. There were two fog periods

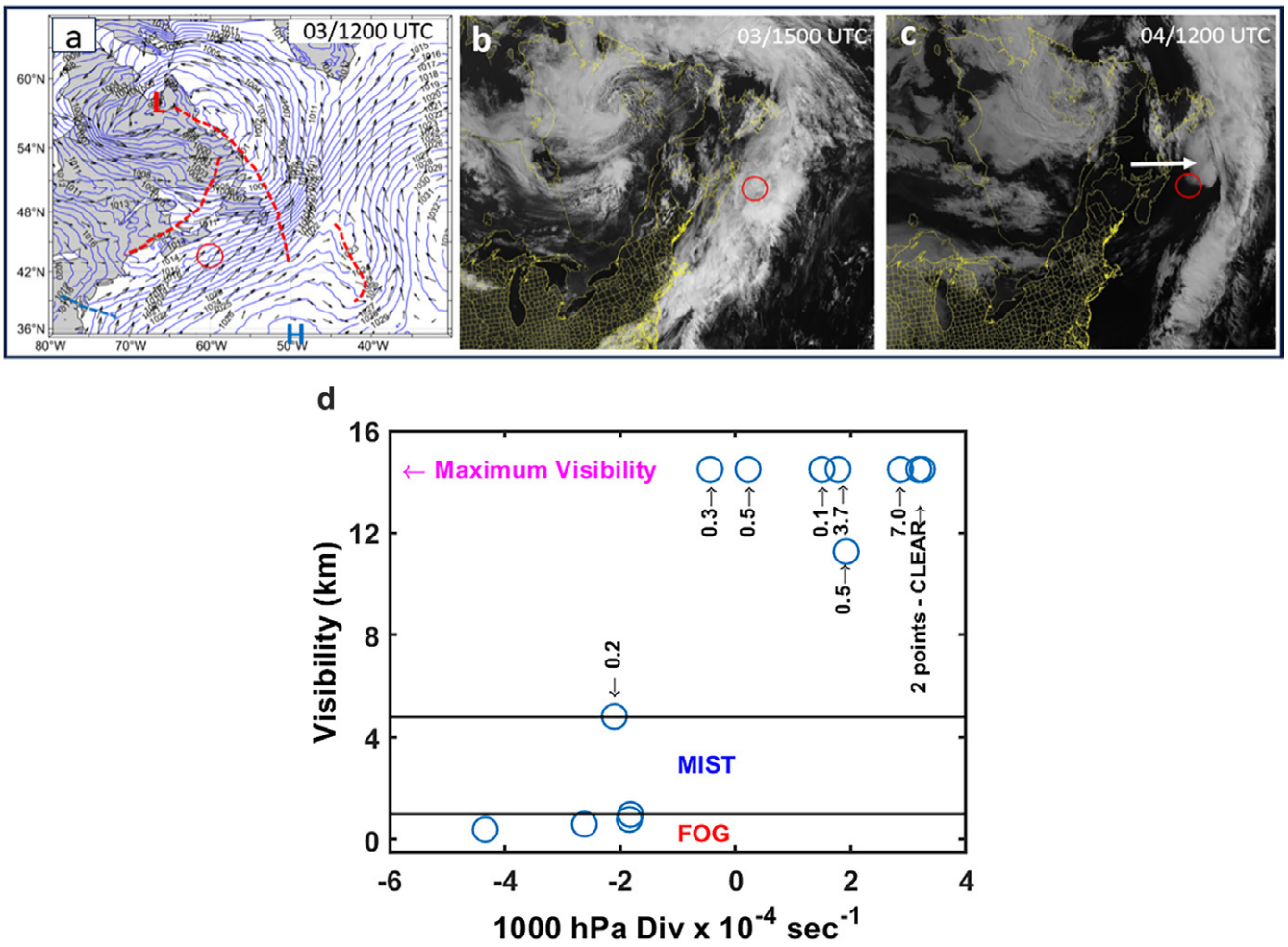

Fig. 7. (a) A plot of the GFS MSLP at 1200 UTC 3 Jul 2022. The term *L* is a deep low pressure on northeastern Canada which dominates Atlantic Canada with a trough (dashed red line) extending to the south along the coastline past Newfoundland. A second trough (dashed red line) extends to the southwest toward the New England coast. The *H* is the center of a high pressure to the south that dominates the surface layer over water. These features cause strong southwesterly surface winds off Atlantic Canada and over Sable (the center of the red circle). (b) GOES east satellite visual image at 1500 UTC 3 Jul. A high-topped cloud band extending from the U.S. Southwest follows the coastline over water, with Sable in fog, through the Labrador Sea, and cyclonically curls around to the center of the low in (a). (c) As in (b), but at 1200 UTC 4 Jul when the cloud band shifted farther east offshore, while anticyclonic conditions cleared the sky over Nova Scotia, the surrounding water, and over a low cloud/fog bank extending from the main cloud band (white arrow) that contained a second fog period at SI that ended soon afterward with clear sky. Almost all July fog at Sable occurred in the presence of a synoptic scale cloud. (d) Visibility in Sable plotted against divergence based on the GFS 6-hourly 1000-hPa data for 0000 UTC 2–5 Jul. Fog visibility <1 km and mist visibility <4.8 km are noted. Posted numbers are the cloud-base ceiling heights in kilometers. Not shown are the ceiling heights of 0.06–0.09 km during fog. CLEAR denotes a cloudless sky. The maximum measured visibility is 14.5 km. The visibility was related to 1000-hPa divergence which was lowest with the most negative divergence (convergence) and fog and was greatest with the most positive divergence and a clear sky. Greater visibility also increased with cloud-base ceiling heights.

within this event, one long (1100 UTC 3 July–0120 UTC 4 July) and the other short (0900–1145 UTC 4 July). At 1200 UTC 3 July, the driving low was centered in northeastern Quebec with a deep trough (low) extending along the eastern coast of Quebec, off the Newfoundland eastern coast, and southward in the Atlantic to 42°N (Fig. 7a); generating strong southwesterly surface winds over most of Atlantic Canada and a concomitant cyclonic cloud band along the Quebec coast; and then extending to the southwest over water (Fig. 7b). This was the first fog period, under a midlevel cloud band. Rawinsondes show that the saturated fog layer included a surface-based air temperature inversion, in the height range of 187–730 m.

With time, the measured sea level pressure (MSLP) trough and cloud band moved eastward. A ridge on the west side of the cloud band began to encroach on the band, lowering the cloud

top. A low cloud–fog bank appendage began to extend out from the cloud band, with the second fog forming at 0900 UTC 4 July. This is evident in the 1200 UTC visual satellite image, extending well out from the sharp, western wall of the band (Fig. 7c). The second fog period had ended 16 min before this image. Sable was on the edge of the cloud bank in this image 5 min before. Rawinsondes show that the fog layer during this second period was a single isothermal layer 170 m deep capped by a dry air inversion. Thus, the two events differed in structure. While details vary, the broad features of the two events were captured by the WRF-ARW simulations (appendix E) such as patchiness of fog and dry inversions aloft the potential fog layer. The visibility during 0000 UTC 2–5 July was directly related to the divergence (Fig. 7d). The lowest visibility and fog occurred with the most negative divergence (i.e., convergence). The maximum visibility occurred with the greatest convergence that triggered surface layer lifting.

b. Aerosols and their evolution—Seeds of fog. A case study representative of size-resolved aerosol processing during IOP9 is shown in Fig. 8. Both MOUDI and nano-MOUDI that capture, respectively, particle sizes ranging from 0.1 to 100 μm (including fog) and from 0.01 to 0.1 μm (ambient aerosols) were used. The samples were chemically characterized using ion chromatography applied to aqueous extracts to yield size-distributed mass loadings of major cations (Na^+, NH_4^+, K^+, Mg^{2+}, and Ca^{2+}) as well as alkylamines such as dimethylamine $DMAH^+$ and diethylamine $DEAH^+$ (Salehpoor and VandenBoer 2023) and anions ($CH_3SO_3^- = MSA^-$, Cl^-, NO_2^-, Br^-, NO_3^-, SO_4^{2-}) (Place et al. 2018). Figure 8 covers the ambient conditions, followed by the onset, persistence, and dissipative conditions of fog.

During the fog event, the mass loading of sea salt ions like Na^+, Mg^{2+}, Cl^-, and sea salt sulfate ($ss\text{-}SO_4^{2-}$) in the coarse mode (1–100 μm) decreased by two orders of magnitude compared to

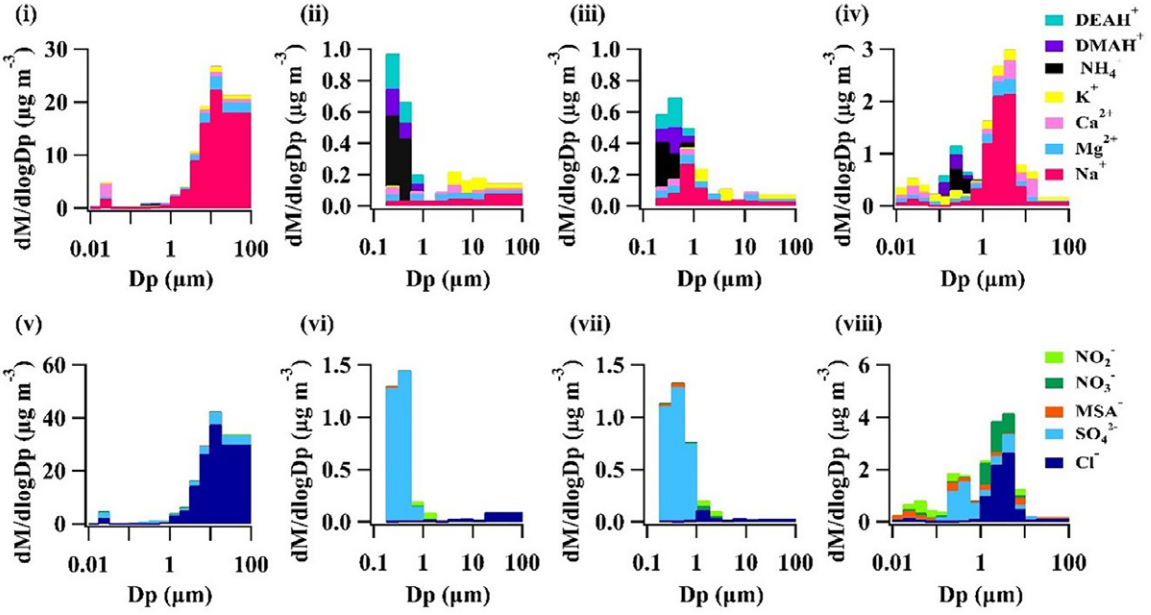

Fig. 8. Ion mass loading (μg m^{-3}) data samples taken near the Sable Island during IOP9 (19–23 Jul) by R/V *Condor*: ion mass loading of major (top) cations and (bottom) anions taken under ambient conditions [prefog; (i) and (v) covering 19–21 Jul], during the fog persistence period sampled during two consecutive intervals [(ii) and (vi) during 21–22 Jul, and (iii) and (vii) during 22–23 Jul] and after the dissipation of fog [(iv) and (viii) during 23–24 Jul] are shown. An MOUDI and nano-MOUDI II were positioned within a weatherproof enclosure mounted to the railing on the deck above pilothouse (~10 m MSL) and were used. Samples were collected using MOUDI during fog events while nano-MOUDI sampled ambient aerosols, both instruments sampling with a flow rate of 30 L min^{-1}. The MOUDI uses nine impaction stages to capture particles of aerodynamic diameters from 0.1 to 100 μm (Chisholm et al. 2021), whereas nano-MOUDI uses additional five impaction stages to collect 0.01–0.1 μm particles. Fifteen samples during fog events and 14 ambient samples were collected with durations spanning 197–2490 min.

prefog conditions due to scavenging and deposition. Following fog dissipation, sea salt aerosols returned, but their mass loadings were lower by a factor of 10 compared to the prefog period. These findings are consistent with the expected role of sea salt aerosols acting as effective FCN, given their high hygroscopicity (Zhao et al. 2022; Sasakawa et al. 2003; Jung et al. 2013). In the fine mode (0.1–1 μm), the mass loadings of reduced nitrogen (NH_4^+, $DMAH^+$, and $DEAH^+$) and processed sulfur (MSA^- and nonsea salt sulfate) increased during the fog event compared to the boundary periods, suggesting that droplets and meteorological conditions supporting fog formation potentially facilitate gases and interstitial aerosol to participate in chemical reactions and gas-to-aqueous partitioning (Ge et al. 2012; Meng and Seinfeld 1994). The mass loading of interstitial aerosol, therefore, increased during fog events and persisted afterward. This confirms the well-known fog scavenging mechanisms of supermicron sea salt aerosols into droplets beyond 20 μm in diameter (Richter et al. 2021; Wagh et al. 2021). The findings are also consistent with marine fog-facilitated gas-particle partitioning recently reported in the Arctic (Kecorius et al. 2023). Upon fog dissipation, supermicron sea salt aerosols were generated faster than their losses and returned to observable levels.

In addition to aerosols >0.1 μm discussed above, attempts were made to characterize bioaerosols using novel, high-resolution detection technologies. Biological species and organic compounds with sizes from tens of nanometers to 100 μm are prevalent in sea spray aerosols (SSAs), thus making nascent growth factors (e.g., hygroscopicity and nucleation) for SSA deviate from pure salt particles (Bertram et al. 2018). The roles of bioaerosols as CCN or FCN are poorly characterized at present (Schiffer et al. 2018), but bioaerosols containing ice nucleating proteins are known to act as ice nuclei and possibly FCNs for rapid mixed-phase cloud/ice-fog formation via heterogeneous processes (Knopf et al. 2018; Huang et al. 2021; Crawford et al. 2020, 2023). Two bioaerosol instruments were deployed: CINCS, a novel instrument designed for sizing, and MBS designed for concentration. Imitating the human lung, CINCS ingests biological cells with minimal stress to the organism, thus maintaining their viability and facilitating postcollection analysis using standard techniques. *Pseudomonas syringae* (PS), known to be conducive for ice nucleation, was selected as the target bioaerosol (Soveizi et al. 2023). Second, MBS is a biofluorescence spectrometer that detects and classifies bioaerosols in real time via the collection of autofluorescence spectra, size, and morphological parameters on a single-particle basis. Following Freitas et al. (2022), MBS data were classified into the following representative groups: weakly fluorescent populations (e.g., SSA with organic content), fluorescent SSAs (FSSAs), highly FSSAs (HFSSAs), primary biological aerosol particles (PBAPs), and nonfluorescent aerosols.

Initial analysis of CINCS data from 25 to 30 July suggested an increased presence of PS on 29 and 30 July (IOPs 13/14) as compared to the other days, suggesting microphysical enhancing capability may have had more of a hand in Fatima-GB rain events as much or more so than the onset/presence of fog [appendix F (i)]. The processed MBS data indicate notable PBAP events during 7–8, 28–29, and 30–31 July and 31 July–1 August, which are consistent with CINCS PS observations [appendix F (ii)]. There are more frequent and extended HFSSA events throughout the deployment. Interestingly, while HFSSA concentrations are generally greater than PBAP, during the PBAP emission events, the PBAP concentration significantly exceeds that of HFSSA. An increase of PBAP during drizzle or rain events is generally evident, while both HFSSA and PBAP are suppressed by fog via nucleation or scavenging/deposition. These observations provide pointers for future multi-instrument interrogations on fog–bioaerosol nexus.

c. Life cycle of fog—Pursuing a stratus-cloud-lowering event. IOP13 encompassed a stratus-cloud-lowering event, a common mechanism of fog formation (Koračin et al. 2001; Fathalli et al. 2022; Singh et al. 2024), as evidenced by synoptic analysis (not shown).

Ceilometer backscatter, Doppler lidar velocity vectors, and contours of vertical velocity variance s_w show that preceding the event (2100 UTC 29 July), the surface winds were southerly with RH of ~85%, while winds aloft were southwesterly/southerly (Fig. 9a). Rawinsondes indicate an unstable surface layer up to ~50 m with an overlying inversion up to ~200 m, topped by a relatively mixed layer up to ~300 m (Fig. 9b). Around 2230 UTC, winds aloft shifted more westerly and a stratus cloud appeared at 600–800 m (Fig. 9a), accompanied by stratus top cooling and temperature inversions beneath (see Singh et al. 2024), as evident from the 2058 UTC sounding (Fig. 9b). Ensuing top-down convection (note the s_w contours) concomitant with light precipitation moistened the lowest 600 m (Fig. 9b, appendix G). Convective turbulent mixing was observed both aloft by the Doppler lidar (Fig. 9a) and at the surface by sonic anemometers (TKE, appendix G). The stratus cloud descended approximately 600 m in 3.5 h (starting 0030 UTC), leading to a dense, persistent, ~125-m-thick fog layer. With the appearance of stratus, turbulence levels decreased and the winds throughout the lowest kilometer shifted westerly.

The fog event was rather homogenous across Sable, based on visibility from the FD70 and BLS900 (appendix G). The significant deviation between BLS900 and FD70 at 1000 UTC was due to the full attenuation of BLS900 signal where lower visibility could not be resolved. The LWC at lower heights during most of the fog event was dominated by larger droplets (10–20 μm) captured by FD70. In combination, FM120 and FD70 data painted a clearer picture of what was occurring, especially near the dissipation of fog just after sunrise (1030 UTC) when the fog layer began to lift (Fig. 9a).

During fog dissipation, TLS captured the profiles of *T*, RH, wind speed (WS), LWC, and the net LW (LWnet) radiation (Fig. 9c). Between 1130 and 1200 UTC, when the fog was still relatively dense, the LWnet profiles showed relatively strong radiative cooling. As the fog dissipation began, the larger droplets evaporated to augment the smaller-particle population and hence an increased LWC (by FM120) and an abrupt drop of visibility (appendix G).

Concomitants were an LWnet profile shift (Fig. 9c) and a tendency toward radiative heating. By 1200–1300 UTC, incoming SW radiation (SWR) further increased, and the concentration of larger droplets disappeared, resulting in a complete evaporation/dissipation of the fog layer. Interestingly, as a result of being optically thin, the fog layer eroded from the bottom (Figs. 9a,c), permitting sufficient surface heating to trigger an increased sensible heat flux and radiative heating over Sable.

d. A tale of the unexpected—Fog shadow. During 1-km resolution COAMPS mesoscale model simulations (appendix H) conducted during 30 June–31 July to support IOP forecasts, a clearing in an otherwise reduced horizontal visibility could be frequently noticed downstream of Sable Island. After 22 July, this phenomenon became conspicuous and was dubbed *fog shadow*. Eight consecutive forecasts starting 1200 UTC 22 July consistently predicted, at least in initial runs, this (unanticipated) phenomenon. For example, in Fig. 10, a large, uniform patch of dense fog (visibility <500 m) is visible to the east of Nova Scotia, in a clearing downstream of Sable Island.

An in-depth analysis of fog shadow, including hindcasts using finer, sub-1-km horizontal grid spacing, will be presented in Gaberšek et al. (2024, manuscript submitted to *Quart. J. Roy. Meteor. Soc.*). The investigator zeal following the observance of fog shadows in simulations led to a super-IOP (IOP10) on 23 July. In addition, fortuitously, R/V *Condor* was slated to sail southward on 22 July to make its final north–south (N–S) transect south of Sable Island across the Gulf Stream, and an intrepid decision was made to change its course for a coordinated (sub)campaign between Sable Island and R/V *Condor* crews to hunt for the fog shadow.

During IOP10, the fog shadow was unequivocally observed, mostly in the early afternoon, by instrumentation at Sable Island and in satellite imagery, with its streamwise length close

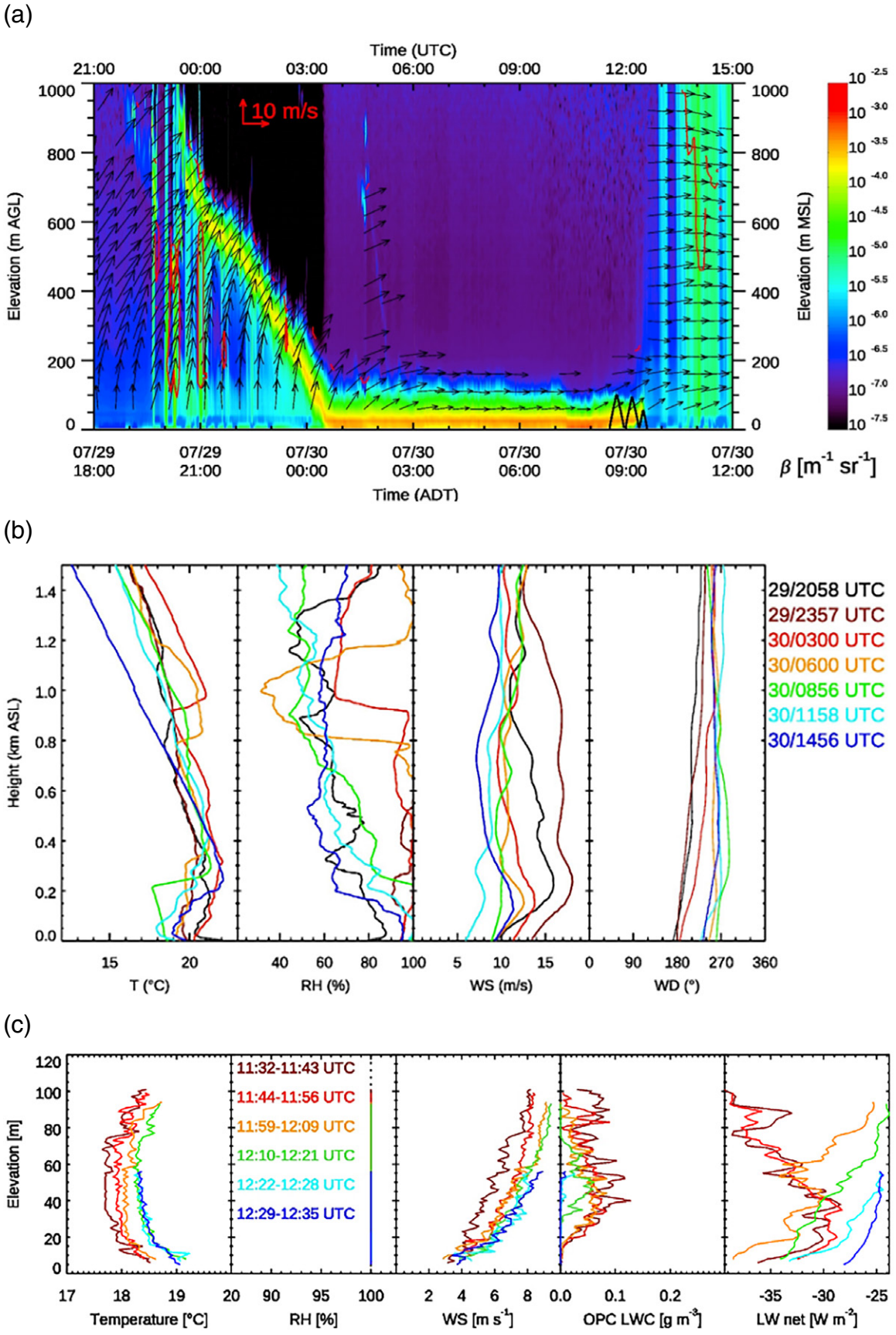

FIG. 9. A cloud-lowering event observed during 29–30 Jul over Sable (IOP13). (a) Time–height cross section of ceilometer backscatter β from the center tower, including Doppler lidar velocity–azimuth display (VAD) horizontal wind fields (black arrows). The flight pattern of TLS is indicated by black sawtooth lines ~1200 UTC, red contours indicate the vertical velocity variance s_w of 0.3 m^2 s^{-2} from lidar vertical stares; (b) vertical meteorological profiles of T, RH, WS, and WD from rawinsondes; (c) TLS profiles with OPC-derived LWC and LWnet from balloon-borne, gimbal-stabilized pyrgeometers, taken during the dissipation phase on 30 Jul.

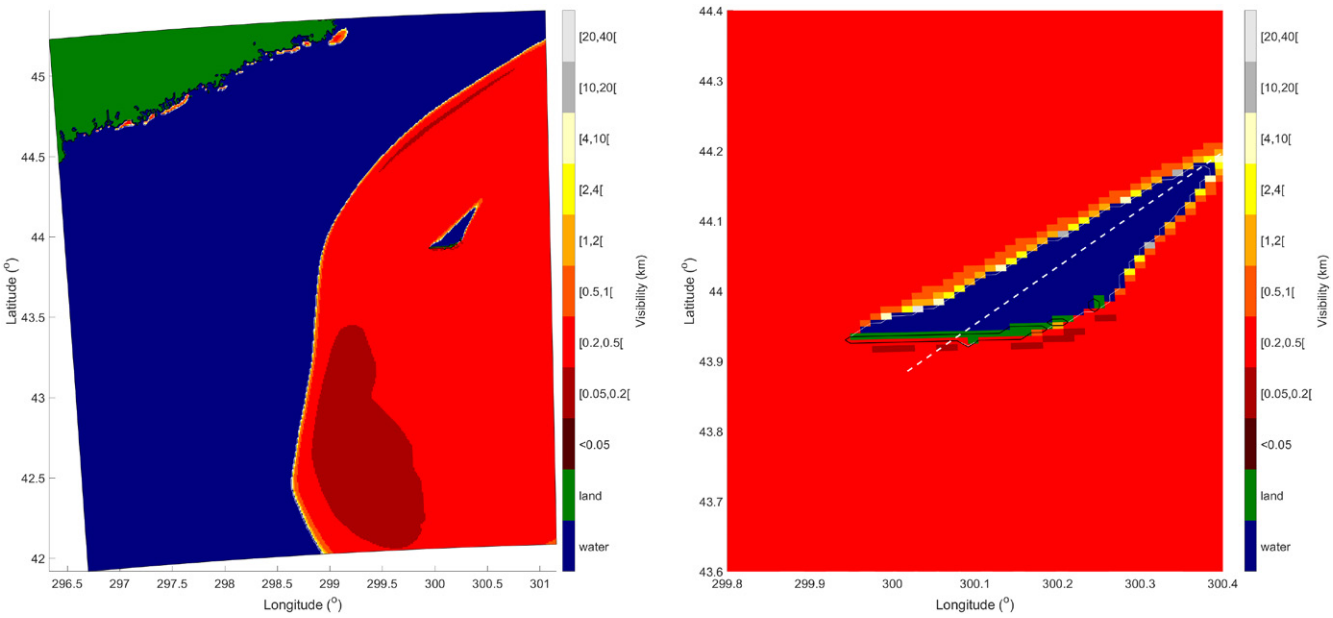

Fig. 10. A 27-h COAMPS forecast of the horizontal visibility at the lowest thermodynamic level (1.5 m) valid at 1500 UTC 24 Jul 2022. (left) A full innermost nest with 1-km grid spacing and (right) an enlarged area centered over Sable. Nests are depicted in appendix H. The dashed white line in the right panel shows the location of the southwest–NE vertical cross section used for studies. A black solid line indicates the coastline, and a white solid line in the left panel represents the fog (appear in red around the island) boundary. At this resolution in the innermost nested grid, Sable Island is barely resolved and the eastern flank of the island is narrower than the rest of the island. It appears as separate small islands in the model because even at 1 km, the grid resolution is too coarse to resolve the actual width.

to the predictions (appendix I). Two mechanisms of fog-shadow genesis were hypothesized, namely, (i) evaporation of fog during (adequate) land surface heating and (ii) increased turbulence as a result of the development of internal boundary layers (IBLs) at the leading and lee edges of Sable. Extensive observations supported the former [discussed in Bardoel et al. (2025)], and thus, the fog shadow here appears to have similarities to fog holes over urban areas due to heat island (Gautam and Singh 2018; Theethai Jacob et al. 2023).

The R/V *Condor* arrived northeast of Sable at the wee hours of 26 July to begin IOP11/ISP5 subcampaign, named "Sable Lee Observing Period (SLOP)," wherein synchronized rawinsonde launches were made, 38 each, from Sable Island and R/V *Condor*. Figures 11a–c provide a measurement summary of SLOP. The data prompted a unique case study of IBLs in the presence of fog and highly localized surface heterogeneity at coastal margins.

While the ship was en route toward Sable, disappointingly, the 24 July forecast made for 26 July was reversed on 25 July, to a no-fog/shadow day, which was prescient. On the Sable, the visibility was in the "mist" regime until 1000 UTC 26 July and the same with occasional fog patches prevailed at R/V *Condor* (Fig. 11e). Thereafter, the visibility at both the ship and Sable was high (~5–15 km), indicating no-fog shadow. Fog appeared on Sable at 2100 UTC 26 July but with high visibility on the ship until 0100 UTC 27 July, thus suggesting a different fog-shadow genesis mechanism than the land heating mechanism above. The ship and Sable captured horizontal (positive) gradients in visibility downstream of the island, which holds implications for IBL effects on fog shadow, optical propagation, and fog–surface interactions. The synoptic conditions, rather than local thermodynamics (Sable heating), seemingly played a decisive role in fog-shadow suppression on 26 July. More details of SLOP study will be presented in Ortiz-Suslow et al. (2025).

e. Fog microphysics via high-resolution simulations. A large-eddy simulation (LES) combined with large-scale dynamics (LSD) and Lagrangian cloud model (LCM)—acronymized

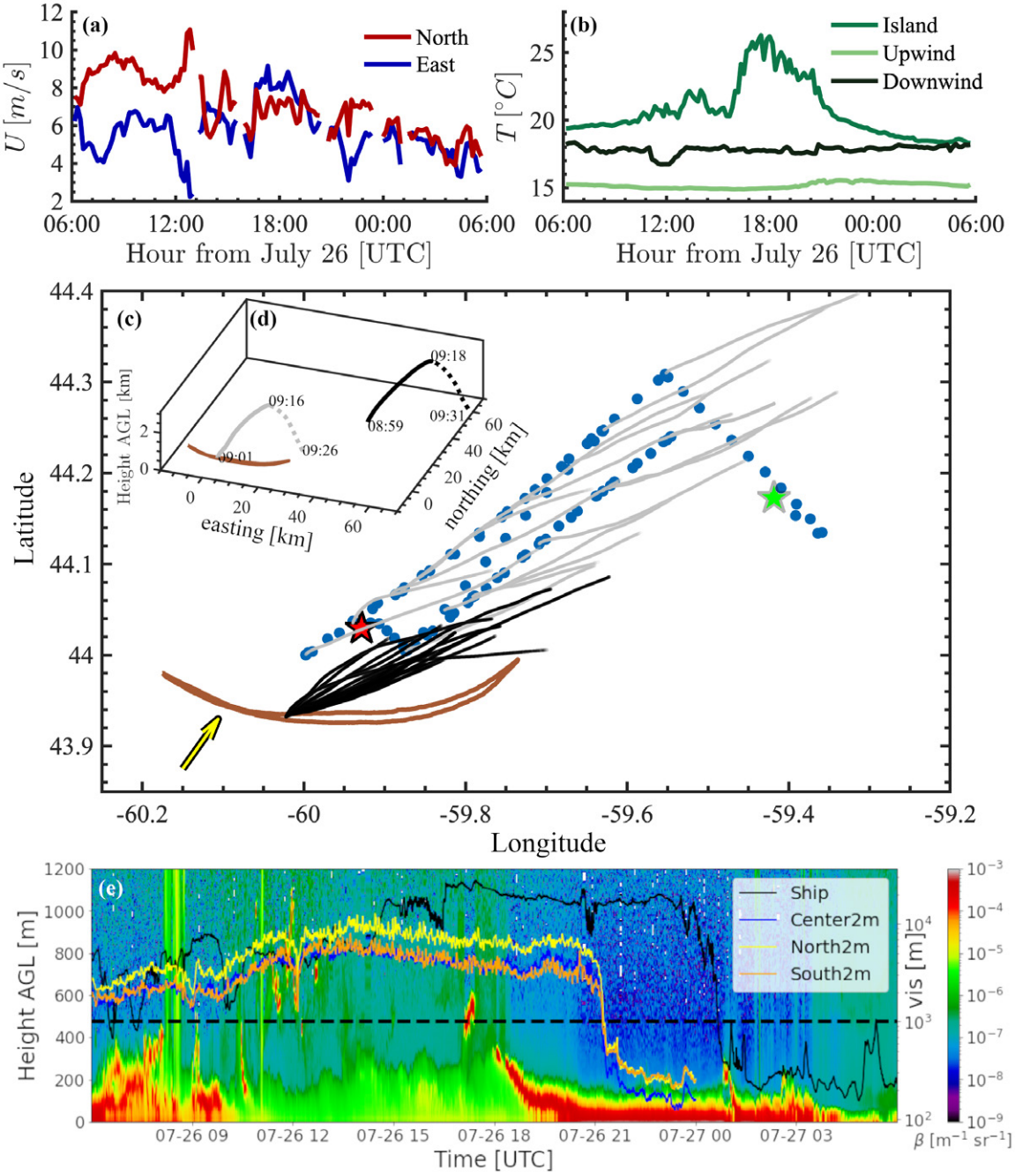

Fig. 11. An overview of SLOP case study, 0600 UTC 26 Jul–0300 UTC 27 Jul. (a) From the R/V *Condor* bowmast, southwesterly surface winds driven by low-level jet that builds through the local morning and then diminishes steadily through the remainder of the IOP were observed; (b) surface *T* records from Sable (radiometric skin *T*, corrected for DWR), a small wave buoy 3 km south of the island (upwind, thermistor on the buoy hull 10 cm from the surface), and R/V *Condor* (downwind, radiometric skin *T* via ROSR); (c) overview of the sampling downstream of Sable, with R/V *Condor* track marked in blue circles. Stars denote the beginning (green) and end (red) positions. The gray/black lines show rawinsonde trajectories from the ship/island, which were deployed in an up–down ABL mode using the controlled leak technique. The black (encircling a white) arrow shows the mean surface wind vector from the ship's bowmast; (d) an example of the coordinated ship (black)–island (gray) up–down rawinsonde launches with distances from West Light station of Sable (brown). (e) Ceilometer backscatter with altitude from R/V *Condor* (color map) overlaid by FD70 visibility at the ship and PWD22s on Sable towers.

L^3 coupling—was used to simulate selected fog events. As an example, the simulation for 13 July (ISP1) is discussed below, with model details briefly in appendix J and in Barve et al. (2025). At the simulation time, R/V *Condor* was on the Hibernia grid (defined later in Fig. 13a). The computations were initialized at 2100 UTC on 11 July with initial

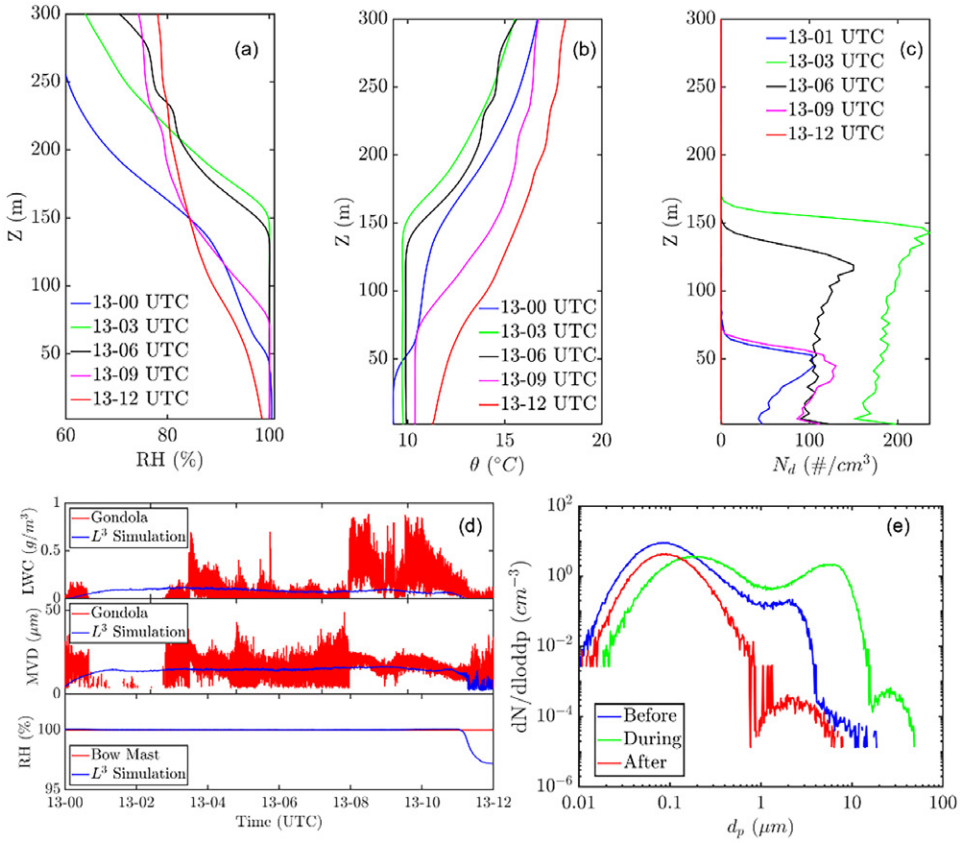

Fig. 12. L³ simulation of R/V *Condor* observations for 13 Jul. (a)–(c) Time evolution of computed horizontally averaged vertical *z* profiles; (d) comparison of measured (using CDP of the Gondola system) and computed microphysical variables at 13-m height; (e) the evolution of droplet size distribution during the fog life cycle. The time-series data are in the day-hour format.

meteorological conditions derived from ERA5 (Hersbach et al. 2023). The initial aerosol distribution was approximated as bimodal, the sum of two lognormal distributions with N_d = 800 cm^{-3}. The simulations continued until 1500 UTC 13 July. As for observations, 12 July showed shallow, intermittent (<50 m thick) fog, with visibility fluctuating above and below 1 km, whereas on 13 July, fog was continuous. Figures 12a–c show the computed evolution of horizontally averaged RH, potential temperature θ, and N_d profiles. Computed LWC, MVD, and RH vis-à-vis, the direct measurements at R/V *Condor* for 13 July are shown in Fig. 12d.

The simulated fog onset occurs ~0100 UTC, defined by LWC > 0.01 g m^{-3} and RH approaching 100%. This is earlier than the recorded observations (0300 UTC). Notwithstanding, the model well replicates the observed fog dissipation time (~1100 UTC). According to Fig. 12a, fog was initially confined near the surface (<50 m), but later, the longwave radiative cooling at the fog top led to top-down convection, contributing to the growth and homogeneity of fog layer, which peaked at 150-m thickness. Figure 12e presents the evolution of droplet size distribution, which was bimodal before and after the fog, but a third peak (at ~8 μm) emerged during fog, indicating the activation of the accumulation mode aerosols that are responsible for increased LWC. Overall, the general consistency of field observations and simulations of LWC, MVD, and RH trends indicates the promise of L^3 as a simulation tool.

f. Nexus of continental shelf turbulence and fog. Guided by the hypothesis that enhanced turbulence over shelf or shelf break favors fog formation due to intensified air–sea interactions and lateral mixing (see appendix A), and since limited measurements during the

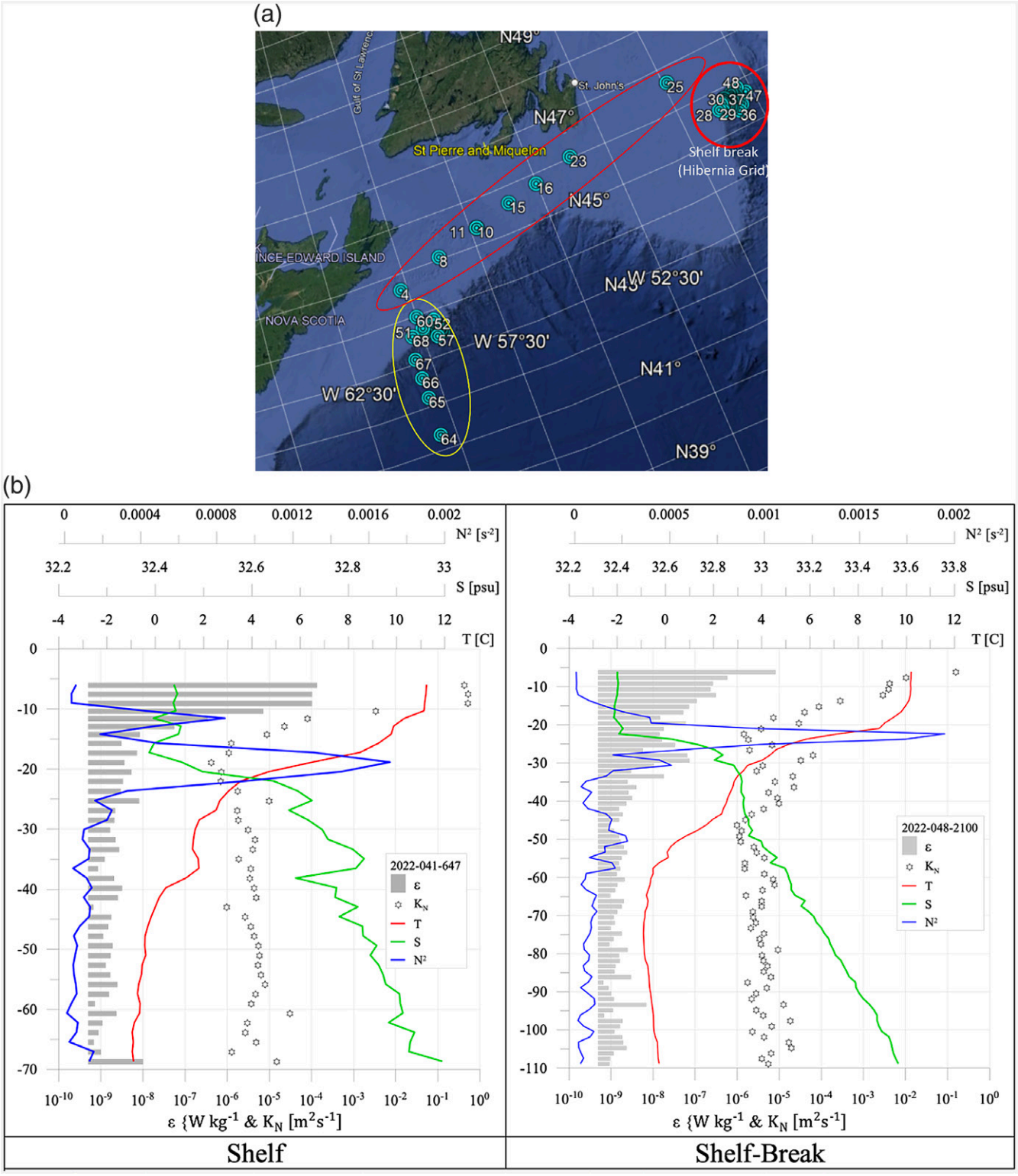

FIG. 13. (a) Locations of VMP-250 stations covered by R/V *Condor*. Stations 4–48 were covered during 8–16 Jul, with stations 4–25 (lighter red ellipse) on the shelf and 26–48 (dubbed Hibernia grid; dark red circle) on both the shelf and shelf break. R/V *Condor* entered Hibernia grid on 0600 UTC ~9 Jul and left at 1900 UTC 16 Jul. 21–31 Jul covered stations 50–68 (yellow ellipse) in the Sable area. Within the Hibernia grid, shelf stations (26, 27, 29–31, 40, 41, and 44) and shelf breaks (28, 32, 39, 45, and 48) were separately analyzed. Some station numbers are not legible because of overlap. (b) Stratification profiles T, S, and N^2 and turbulent variables ε and K_N at the Hibernia grid [for details, see (a)]. The vertical axis is the depth (m) below the mean sea surface located at $z = 0$. The T, S, and depth z are from the VMP-250, and ε was evaluated using shear profiles. The term K_N was calculated using the standard techniques (Lozovatsky et al. 2021).

2018 C-FOG field campaign to the south of Nova Scotia could not fully verify this hypothesis (Lozovatsky et al. 2021), further measurements were conducted in the Hibernia region of the Newfoundland shelf and across the Nova Scotia (NS) shelf not far from the Sable and toward the Gulf Stream cold wall. Uprising VMP-250 was used for hydrophysical and turbulence measurements at 68 stations (Fig. 13a). The data analysis on the Hibernia grid reported here consisted of shelf and shelf-break stations.

Characteristic station-averaged profiles of temperature $T(z)$, salinity $S(z)$, and buoyancy frequency $N^2(z)$ and the profiles of TKE dissipation rate ε and eddy diffusivity estimated using $K_N = 0.2\varepsilon/N^2$ (Lozovatsky et al. 2021) are shown in Fig. 13b. The near-surface turbulence on the shelf break ($\varepsilon \approx 10^{-5}$ m^2 s^{-3} and $K_N \approx 10^{-1}$ m^2 s^{-1}) was weaker compared to that on the shelf (10^{-4} m^2 s^{-3} and 1 m^2 s^{-1}). The cumulative distribution functions (CDFs) of the diffusivity K_N calculated using datasets of eight shelf (over the depth range $-65 < z < -30$ m) and five shelf-break ($-90 < z < -30$ m) stations, with depth ranges encompassing the thermocline, could be approximated by the generalized extreme value distributions, as was for the NS shelf (Lozovatsky et al. 2021), but parameters of the distributions were drastically different (not shown). The median diffusivity for the Hibernia shelf was 4.1×10^{-6} m^2 s^{-1}, only slightly below the shelf-break diffusivity of 5.3×10^{-6} m^2 s^{-1}, and both were much lower than diffusivities at the Nova Scotia shelf (3×10^{-5} m^2 s^{-1}) and shelf break (5.8×10^{-5} m^2 s^{-1}) during C-FOG. R/V *Condor* encountered fog recurrently within the Hibernia grid (see ISP1 and ISP2), but a definite association of fog prevalence and surface or thermocline turbulence awaits further data analysis.

7. Exploring Frontier technologies

The following are examples of novel measurement technologies attempted during Fatima-GB: (i) simultaneous vertical profiling of microphysics and turbulence above the sea surface using C-CAMS (Fig. 2) and (ii) the Super Combo (Figs. 3h,i) for the measurement of TKE (at K scale) and temperature fluctuation dissipation (O–C scale).

a. C-CAMS. A major design challenge of C-CAMS was to obtain a motion-stable platform to safely mount research-grade sensor payloads of larger size, weight, and power supply tethered to a crane wire to allow sampling at different heights above the sea level at a distance uninfluenced by the ship hull. The solution was a reinforced fiberglass pallet container mounted with a horizontal 10-ft tower section to overhang meteorological instrumentation above the ocean surface. The instrument suite characterized the near-surface visibility, meteorology, thermodynamics, turbulence, and microphysics. C-CAMS measurements on 14 July 2022 (super-IOP5) are shown in Fig. 14, highlighting its capability of sampling a range of variables. Also overlaid are the data from D-CAMS and from the ship bowmast to extend the vertical data coverage.

The visibility measurements show that fog extended above the level of D-CAMS. In fog, C-CAMS visibility increased toward the surface. Of interest is a stably stratified surface layer ($\overline{\theta}$ profile) accompanied by an increase of water vapor with height in both clear and foggy conditions. Since the clear condition is at near saturation (RH = 95%–98%), significant increases of T with height resulted in an "anomalous" vertical gradient in the mixing ratio r under stable clear conditions, and the increase of r with height is consistent with observed negative latent heat fluxes. In the fog case, the near-surface upward water vapor fluxes are at odds with previous measurements, which call for further study by invoking the role of stable stratification. Large negative sensible heat fluxes were identified in both conditions, consistent with the stable T gradient near the surface. Significant vertical gradients are evident for all three fluxes, particularly for the momentum flux, in both fog and clear conditions, a clear

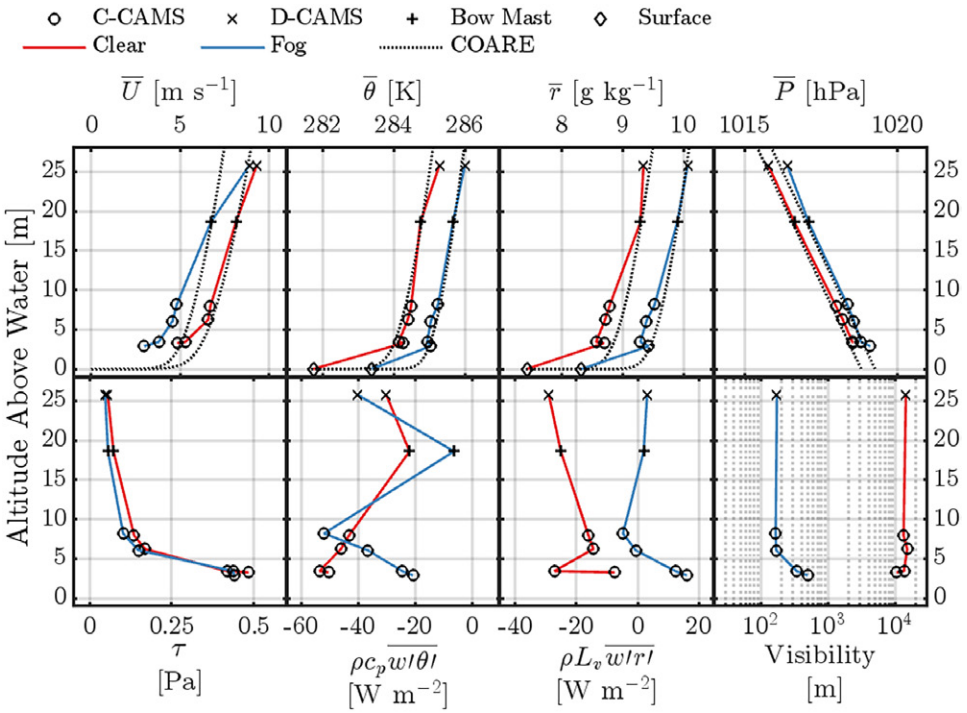

FIG. 14. C-CAMS measured vertical profiles of bulk meteorological parameters (mean values of WS $\overline{U}$, potential temperature $\overline{\theta}$, water vapor mixing ratio $\overline{r}$, pressure $\overline{P}$, momentum flux τ, sensible heat flux $\rho c_p \overline{w'\theta'}$, latent heat flux $\rho L_v \overline{w'r'}$, and visibility) (for C-CAMS details, see Fig. 2, et seq.). The figure shows measurements (circles) on 14 Jul 2022 during clear (red) and foggy (blue) conditions at 1602 UTC and 1950 UTC, respectively, during the nominal 1-h deployment periods. The bowmast (+) and D-CAMS (×) data are added to extend the altitude to 18.6 and 25.4 m above the water level, respectively. The bowmast and D-CAMS data are time averaged over the entire C-CAMS sampling period, while each C-CAMS data point represents 10 min averaging during stable and level sampling at three discrete heights. As well, the SST and derived sea surface mixing ratio are shown in the $\overline{\theta}$ and $\overline{r}$ profiles. The bowmast and shipboard ROSR data were used as inputs to the COARE 3.0 algorithm (Fairall et al. 2003) to obtain canonical mean profiles shown with dotted lines in the top row.

violation of the constant flux surface layer assumption. Further details on C-CAMS will be presented in Yamaguchi et al. (2025).

b. Super Combo—A probe system for penetrating dissipation scales of MABL turbulence. The "Super Combo" (Figs. 3h,i) is an assemblage of high-resolution probes for simultaneous direct measurement of dissipating (K and O–C) microscales, with additional information retrievable on LWC, MVD, and N_d. The probe system was on a gimbaled platform, controlled by a neural network to align the probes in the wind direction, a requirement for hot-wire probe operation (Kit et al. 2017). All hot wires were operated in constant temperature anemometry (CTA) mode. The technique developed by Goldschmidt and Householder (1969) for wind tunnels was adopted that converts voltage fluctuations needed by CTA to maintain its temperature upon impaction of droplets into droplet parameters.

Figure 15 shows a representative dataset of 1-min-averaged visibility (teetering at the fog threshold), directly measured TKE dissipation rate ε, and microphysical parameters. Compared with conventional instruments, FM120 in particular, the Super Combo is able to capture trends of microphysical parameters at a higher space–time resolution. Measured MVD and LWC are on comparable scales with FM120. The Super Combo gives N_d approximately one order of magnitude higher than that of the FM120, likely due to its higher sensitivity to small droplet sizes. Further details will be presented in K. Huang et al. (2025, unpublished manuscript).

8. Summary and challenges

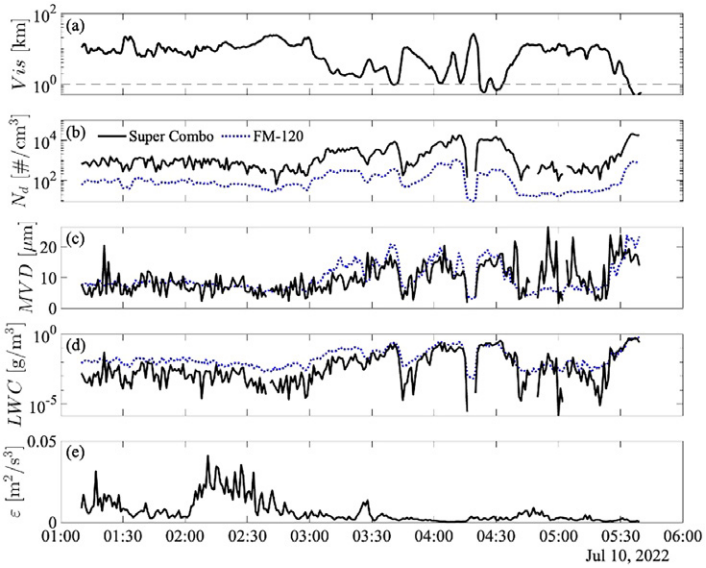

FIG. 15. The Super Combo system uses a sonic anemometer to measure larger scales and a fine-wire probe assembly on a platform that rotates to align with the flow direction to measure the turbulence. The probe assortment consists of high-resolution sensors—two X wires (TSI 1241-20 film), one parallel array probe (Dantec 55P71 film), and two nanoscale cold wires [temperature nanoscale thermal anemometry probes (T-NSTAPs)]—all collocated with a sonic (RM Young 81000). Shown in the figure are the (a) visibility Vis from FD70 and representative time-series measurements from the Super Combo system taken on 10 Jul (IOP3). Gray dashed line in (a) represents the threshold visibility of 1 km. For comparison, (b)–(d) data from FM120 are included with dotted lines. Super Combo can resolve droplets (~1 μm) smaller than that by FM120 (~2–5 μm) and hence the measurement disparity. As expected, low Vis corresponds to higher N_d and lower levels of turbulence.

Prediction of marine fog is one of the most challenging endeavors in meteorology, due mainly to strong (bio)physicochemical interactions spanning 15 decades of space–time scales that underlie its life cycle. Paucity of knowledge, lack of adequate relevant high-fidelity data due to measurement difficulties across synoptic to submicron scales in logistically challenging environments, and nonstationarity and inhomogeneity of marine fog have stymied the progress in fog research, notwithstanding important applications of fog forecasting in transportation, agriculture, industrial, and defense sectors. Fatima-GB was a comprehensive multidisciplinary field campaign augmented by NWP modeling and high-resolution (research-grade) simulations to study fog in shallower, noncoastal waters—categorized as sea fog. The study mainly covered the Grand Banks area on the North Atlantic shelf, one of the foggiest places on Earth in the summer. Access to an isolated islet (Sable Island) south of Grand Banks, located in the advection pathway of warm Gulf Stream air toward colder Grand Banks water conditioned by Labrador Current, helped study both sea fog life cycle and fog–turbulence–land interactions. A ship (R/V *Condor*) and Sable Island were densely instrumented with an unprecedent array of sensors that collected an extensive set of data. Some novel sensors/sensor systems were among those deployed. Data analysis showed that the long-held hypothesis that advection of warm air over colder water causes marine fog was oversimplistic, and a synoptic trigger (e.g., moving high–low systems) is needed for fog genesis. Upper-ocean turbulence measurements cast another hypothesis into doubt that (intense) shelf-break turbulence may favor air–sea interactions and sea fog. Study of cloud-lowering events shaped by low-level convergence/divergence illustrated the importance of finer details of meteorological and turbulence structure, highlighting the role of subgrid microphysical processes of NWP in predicting sea fog. First-ever long/shortwave radiation balance measurements at the fog top using an instrumented tethered balloon system opened up new avenues for future numerical/theoretical studies on fog-top convection and its interaction with surface turbulence during fog evolution. FCNs are imperative for fog, and chemical analyses illustrated that 1–100-μm-sized coarse (hygroscopic) sea salt aerosols facilitated sea fog but were removed by scavenging during fog evolution, leaving behind compounds that might have formed due to chemical reactions between gases and interstitial aerosols. Novel bioaerosol sensors adumbrated some association between hydrometeors and bioaerosols and broached future opportunities for

delineating the role of (~10-nm scale) bioaerosols as FCNs, a topic that has invited debate. Overall, accounting for such biochemophysical processes in microphysical schemes of NWP models will be a captivating research topic for the future. Prompted by NWP modeling, a coordinated subcampaign between the groups at Sable Island and R/V *Condor* uncovered the "fog shadow" phenomenon—a clearing in the wake of an island in an otherwise foggy area. The existence of tens of kilometer-sized fog shadow behind the ~1-km-long Sable Island was confirmed for some days. Fog shadow was a result of differential surface heating between the island and the surrounding ocean but was sensitively modulated by synoptic conditions and internal boundary layers. While COAMPS modeling was the first to elicit fog shadow, the onset and disappearance times of fog shadow in the model had disparities with observations, which is a topic for future research.

Acknowledgments. Fatima-GB was an ambitious "big-science" project that was only possible through international scientific cooperation; involvement of a bevy of diverse, skilled, and dedicated personnel; munificent support of many organizations; and a special multidisciplinary funding mechanism. Daniel Gibson, Rodrigo Menafra, Gregory Siddall, and Scott Simone of the Canadian National Network of Centers of Excellence (MEOPAR) shepherded the utilization as well as the conversion of deep-sea supply vessel *Atlantic Condor* to a research vessel. ONR Naval Vessels Program Manager Rob Sparrock facilitated the renting of the vessel. The support and beneficence of Jason Surette (operations manager) and his colleagues (Mathieu D'Astous, Greg Stoud, and Sarah Medill) at the Sable Island National Park Reserve were vital for the Sable Island campaign. The Sable Science Lead Cornelia (Nell) den Heyer of the Bedford Institute of Oceanography for Fisheries and Oceans, Canada, helped gaining access to electricity and accommodation resources at the island. Brilliant logistician Marvin Willis carried a heavy load, from renting a hangar at the Halifax Airport as the operations center to arranging charter flights, helicopters, and sea lift/barges (from Sable Air and Air Borealis, Vision Air, and Dominion Diving, respectively) to the timely replenishing of food supplies and hardware at Sable Island and R/V *Condor*. He was joined by Paul LeBlanc, who resided partly at Sable Island, to ensure smooth operations. Shawn Quinn of Compliance in Moton Inc. (CiM) was relegated to safety and compliance of transported items. Reno Sit of ECCC led instrumented UAV operations, and Alexis Trottier-Pacquet, Evan Newman Lauren Robinson, Phillipe Gauvin-Bourdon, Baban Nagare, and Minghong Zhang were part of the Fatima support group. This work was funded by Grant N00014-21-1-2296 of the Office of Naval Research (see appendix A). Additional support was provided by the Wayne and Diana Murdy Fund at UND and the administrations of UND and UU. Finally, we extend our sincere appreciation to ONR program managers Dan Eleuterio (who also contributed to this manuscript), Josh Cossuth, and Kate Mulreany for their crucial assistance in numerous ways.

Sadly, one of the Fatima team members, Professor Iossif Lozovatsky, who prepared Fig. 13, passed away unexpectedly on 23 December 2023. We dedicate this paper to his memory and celebrate his contributions to physical oceanography over the past four decades.

Data availability statement. The data used herein have been collected by four research groups (UND/PSL-NOAA, NPS, UU, and Scripps/UCSD) consisting of PIs as well as five collaborating groups (DU, YorkU, AFIT, UMAN, and OntTechU); see appendix A for acronyms. All data are available in a single shared Google Drive at UND with metadata. A backup drive is also maintained. After an embargo period for the PIs to conduct research, all data will be available to the scientific community after 1 August 2025, unrestricted. This database includes raw, intermediate, and QC/QA data, COAMPS and WRF hourly outputs (plots), satellite data, and daily weather forecasts from multiple sources.

Appendix A
General Project Information and Summary Hypotheses

The Fatima project seeks leaps in the fundamental understanding of sea fog (SF) via multidisciplinary research. It was funded under a Multidisciplinary University Research Initiative (MURI) of the Marine Meteorology and Space Weather Program of the Office of Naval Research (2021–26). The *objectives* are to understand and quantify processes underlying the life cycle of SF and represent them in NWP models via (i) deploying leading-edge instrumentation, including novel measurement technologies, to probe from synoptic to smallest scales of ABL turbulence (i.e., K and O–C scales ~1 mm) and aerosols (~10–100 nm); (ii) theoretical/numerical analyses of two-phase turbulence; (iii) delving into droplet/aerosol microphysics and dynamics, thermodynamics, surface processes, and forcing; (iv) developing microphysical parameterizations for improved visibility predictions using NWPs; and (iv) studying impacts of fog on electro-optical propagation. Seven guiding hypotheses were used:

1) Warmer humid airflow along negative SST gradients, in collusion with sea surface cooling by air–sea fluxes, provides favorable conditions for SF. Air–sea interactions are abetted by enhanced upper-oceanic turbulence (e.g., shelf/shelf-break mixing). Synoptic forcing on the ABL is also a key factor.
2) Unlike for low-level (e.g., stratocumulus) clouds, sea surface processes control the fog life cycle through air–sea fluxes and ABL dynamics (in particular wave boundary layer, LW/SW radiation, and shear). FCNs are significantly contributed by sea surface aerosols (SSAs) produced by wave breaking.
3) Precipitation from clouds above the fog layer has profound impacts on SF life cycle by moistening the subcloud layer, scavenging fog droplets, suppressing SSA production, and modifying surface waves and turbulent fluxes.
4) While synoptic to microscales strongly affect SF genesis, a critical (rate determining) step is outer (integral) scale eddies feeding TKE to K scales via Kolmogorov (nonlinear) energy cascade down the inertial subrange. It is within K eddies that temperature/moisture homogenizes and spawns fog droplets around embedded FCNs by vapor deposition under specific conditions.
5) Radiative cooling and heating are crucial for the life cycle of SF through their link to microphysical and turbulence processes.
6) Optical attenuation in fog can be parameterized using fog-integrated microphysical and turbulence parameters.
7) A two-wavelength microwave (MW) and near-infrared (NIR) scintillometer can be used to infer the microphysical properties of fog, forms of precipitation, and evolutionary stages of fog.

Fatima enlists a multidisciplinary team of researchers for melding theory, simulations, field observations, technological developments, and NWP modeling. It is led by five universities: University of Notre Dame (UND), Naval Postgraduate School (NPS), Scripps Institute of Oceanography, University of California, San Diego (Scripps/UCSD), University of Utah (UU), and University of Minnesota (UM). Collaborating institutions from the United States are the the Airforce Institute of Technology (AFIT), Argonne National Laboratory (ANL), Army Research Laboratory (ARL), Pacific Northwest National Laboratory (PNNL), and the Physical Sciences Laboratory at NOAA (PSL-NOAA). The international participants are Bedford Institute of Oceanography (BIO), Canada; Dalhousie University (DU), Canada; Digital Environment, WSP Canada (WSP); Korea Institute of Ocean Science and Technology

(KIOST), South Korea; University of Manchester (UMAN), United Kingdom; Ontario Technical University (OntTechU), Canada; Yonsei University (YU), South Korea; and York University (YorkU), Canada.

Appendix B
Grand Banks and Sable Island—Domain Covered by R/V

A backdrop of Fatima-GB campaign with ocean and land domains covered is shown in Fig. B1, including measurement platforms.

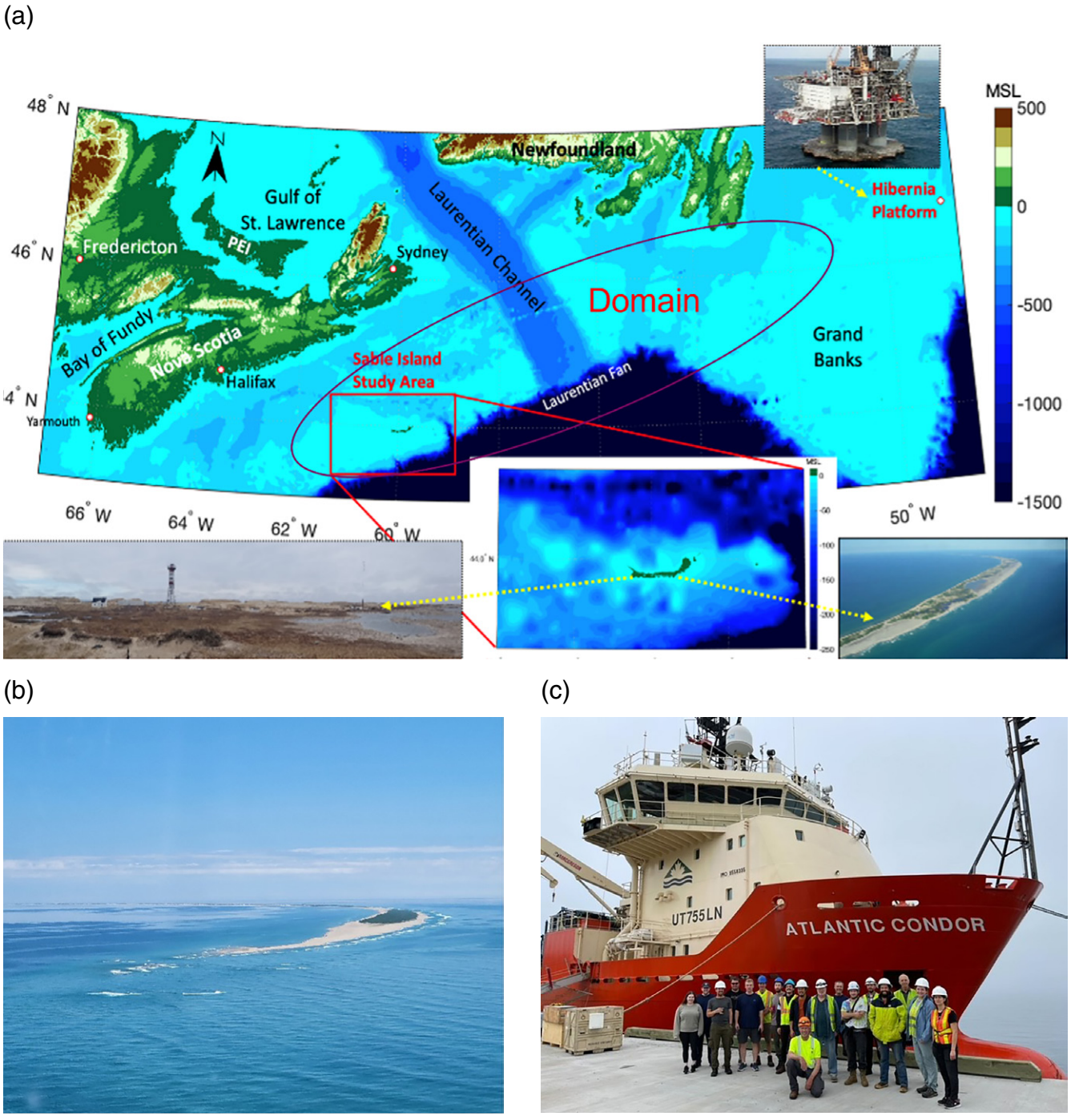

Fig. B1. (a) The study domain in North Atlantic for Fatima-GB. The main sites were the SI and Grand Banks, with a lesser (satellite) site at the Hibernia Oil Platform. (b) SI (43.9337°N, 59.9149°l W at the center) as viewed from an approaching aircraft. Sable is located 300 km southeast of Halifax, Nova Scotia, Canada. (c) The R/V *Condor*, which carried 18 scientists and 12 crew members for Fatima-GB.

Appendix C
Instrument Layout at Sable Island

An extensive array of instruments at Sable was packed into two clusters, as shown in Fig. C1.

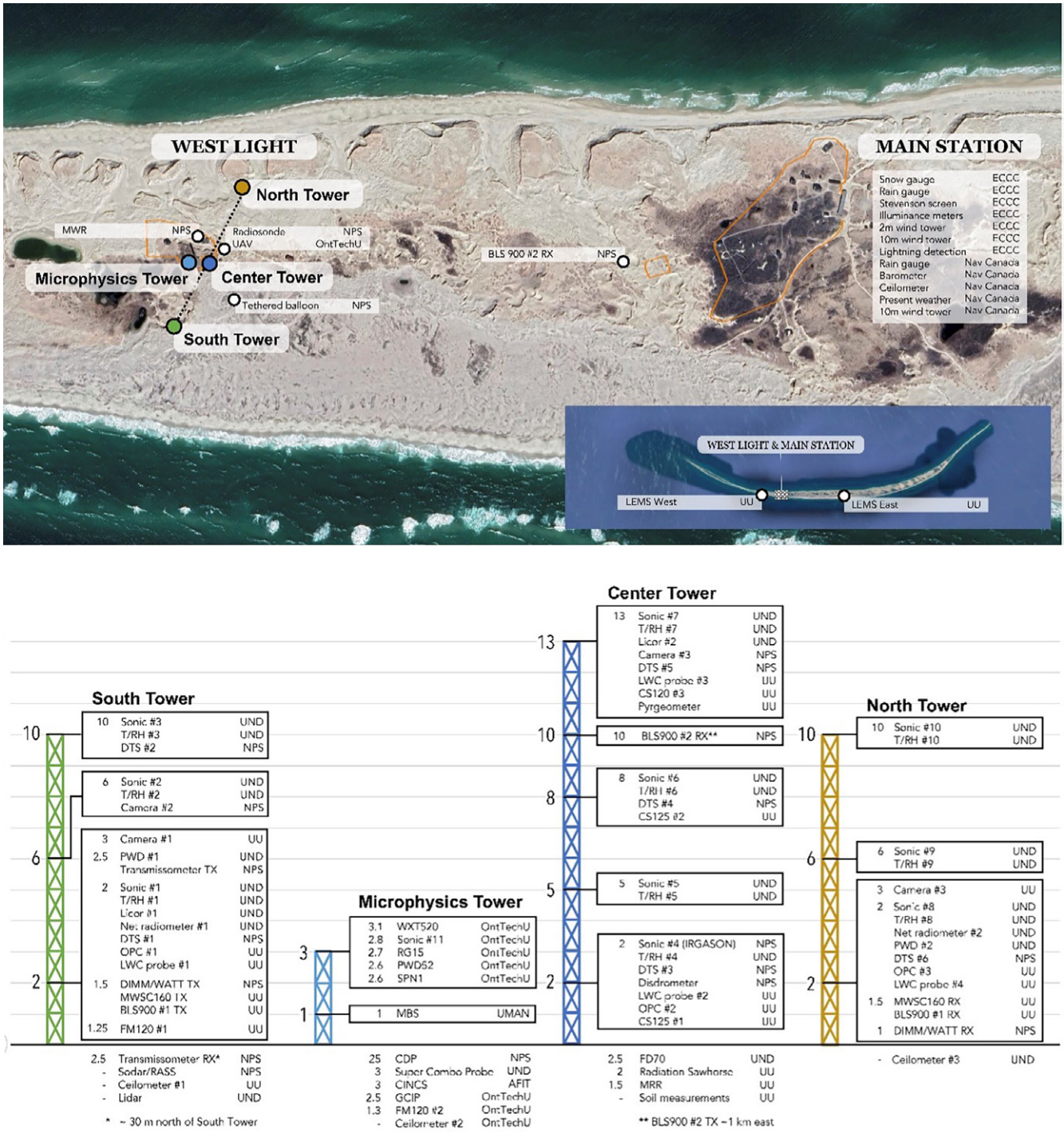

Fig. C1. (top) Two principal campaign locations—West Light and Main Station. Backbone of towers in West Light (south, center, microphysical, and north) around which instrumentation is clustered. Default Parks-Canada instruments in Main Station from Environment and Climate Change Canada (ECCC) and NAV Canada. Inset: LEMS locations, with the shaded rectangle denoting the zoomed-in area. (bottom) Instruments on each tower and their location, with surrounding instruments in each cluster. All heights (numbers) are in meters, and instrumentation is described in the text and appendix K.

Appendix D
Hourly Aerosol Concentration Statistics

The 25th percentile (p25), 50th percentile (p50), 75th percentile (p75), mean, and standard deviation (std) of hourly aerosol concentrations for aerosols with diameters larger than 10, 100, and 200 nm during fog and no fog at R/V *Condor* are presented in Table D1.

Table D1. Statistical data on hourly aerosol concentration.

	N_10_fog	N_10_nofog	N_100_fog	N_100_nofog	N_200_fog	N_200_nofog
No./cm^{-3}	Fog	No fog	Fog	No fog	Fog	No fog
p25	329	358	125	152	33	44
p50	565	828	251	317	85	74
p75	904	1229	448	517	129	115
Mean	630	831	300	361	91	94
SD	349	517	207	255	66	75

Appendix E
WRF Simulation of IOP1, Illustrating Synoptic Influence on Fog Genesis

Following the identification of synoptic trigger in fog formation during IOP1, WRF V3.9.1 with the Advanced Research version of WRF (ARW) dynamical solver (Skamarock et al. 2008) was used for detailed studies of relevant physical processes. Therein, six Lambert projection nested domains with a parent-to-child horizontal resolution ratio of 3:1 and resolution from 40.5 km to 500 m were used. Modifications were made to the static data of topography and land use to accurately capture the details of Sable Island. Two arc-second digital elevation datasets were implemented: Shuttle Radar Topography Mission (SRTM 1) (NASA; https://lta.cr.usgs.gov/SRTM1Arc) and North American Land Cover Monitoring System (NALCMS)_2015_30m data (USGS; https://www.cec.org/nalcms). The NALCMS 19 classes were adapted to the modis_landuse_20class_30s_with_lakes land-cover data; for a full description of the general procedure, see Vladimirov et al. (2018). The model was implemented with 50 pressure-based terrain-following vertical levels with more levels in the lowest 1 km. The model top was set to 50 hPa. The initial and boundary conditions were derived from the 0.25° × 0.25° NCEP Final Operational Model Global Tropospheric Analyses (https://rda.ucar.edu/datasets/ds083.3/) with datasets available every 6 h. The option for grid nudging (fdda) was used only for the outermost domain 1 (D1) for all vertical levels. The simple ocean mixed-layer model following Pollard et al. (1972) was activated as a model option to provide SST.

The WRF physics package included the Radiative Transfer Model parameterization (Mlawer et al. 1997) for LW and the Dudhia (1989) scheme for SWR to compute radiation every 1 min; the Noah land surface model (Chen and Dudhia 2001); and the Grell–Freitas cumulus parameterization, for the first two domains only (Grell and Freitas 2014). The same configuration was used in Dimitrova et al. (2021) covering the identical area. Therein, different microphysical and planetary boundary layer (PBL) parameterizations were compared and the two-double-moment option of the National Severe Storms Laboratory (NSSL) microphysics scheme (Mansell et al. 2010) was found to perform better than alternative schemes tested, when used with both nonlocal (Yonsei University; Hong et al. 2006) and local (Mellor–Yamada, Nakanishi, and Niino level 2.5 parameterizations; Nakanishi and Niino 2006) PBL schemes. Therefore, the same NSSL microphysics and Shin–Hong PBL schemes (Shin and Hong 2015), coupled with the revised MM5 Monin–Obukhov surface layer scheme (Jiménez et al. 2012), were selected for Fatima-GB simulations. The new Shin–Hong PBL scheme has been developed to address the so-called gray zone challenges by using scale-aware PBL parameterizations;

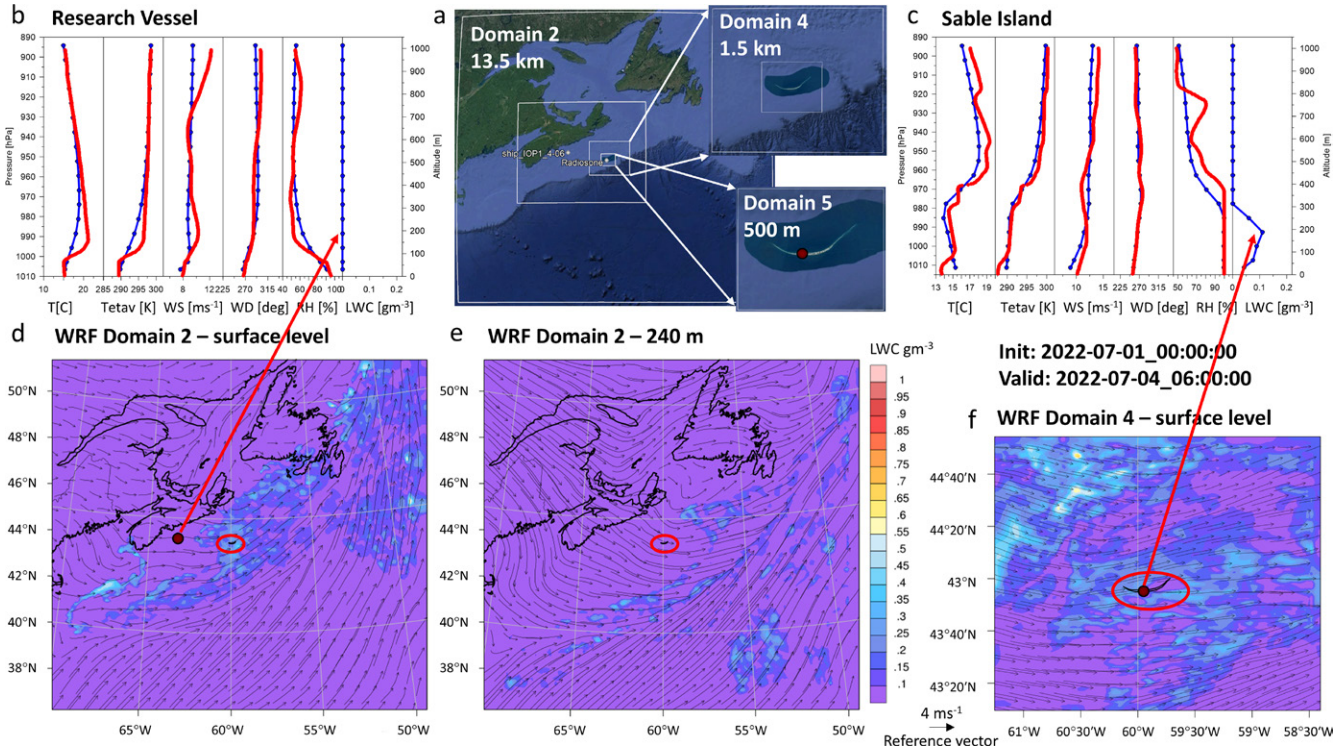

Fig. E1. (a) Domains used for WRF simulations, (b) simulated vertical profiles of main meteorological variables compared with observations from R/V *Condor* located in domain 2 (red—observations, blue—simulations); (c) observations vs simulations from Sable Island located in domain 5; (d) horizontal sections of LWC at the surface level for domain 2; (e) LWC for 240-m elevation for domain 2; (f) surface level for domain 4 showing that LWC or fog is confined beneath an inversion layer. The surface velocity vectors are westerly/southwesterly at Sable Island. (d),(f) Simulations were started at 0000 UTC on 1 Jul, and the plots shown are at 0600 UTC 4 Jul. Sable Island is encircled by a red ellipse and R/V *Condor* by a red circle. No fog was observed at R/V *Condor* during this IOP at Sable Island (Fig. 4).

they implement scale-dependent vertical transport in convective conditions and vertical mixing in the stable PBL and free atmosphere.

WRF results of IOP1 are presented in Fig. E1, in the context of synoptic triggers discussed in Fig. 7 of the paper. For brevity, a time (0600 UTC 4 July) between the long and short fog periods is presented. The simulation results are in reasonable agreement with the data taken at R/V *Condor* and Sable Island. Synoptic conditions prior to fog formation were a deep low-pressure center over northeast (NE) Canada with a trough that extended along the Atlantic coast and over Sable Island with strong southwesterly winds and a broad cloud band, in agreement with Figs. 7a and 7b. An eastbound ridge encroached existing surface moisture and clouds, causing fog. Fog coverage followed the line of convergence below the inversion layer (also see Hintz et al. 2024). Fog formation was most likely due to the convergence of the flow within a thin marine boundary layer topped by an inversion layer (domain 4) as discussed in Fig. 7d. The presence of deeper isothermal layers topped by dry inversions as a precursor to the second fog event was also evident from domain d04 simulations.

Appendix F
Delving into Recondite Bioaerosol Connection

(i) AFIT/NPS deployed CINCS, a unique instrument that was specifically adapted for bioaerosol detection. CINCS consists of two primary components: (i) uniquely engineered liquid spot sampler (LSS) that "gently" ingests ultrafine through coarse-mode aerosols (ranging in size from 5 nm through 10 μm) and (ii) electrochemical detection sensor (EDS) that employs square-wave voltammetry (SWV) and electrodes treated with antibodies specific to

bioaerosol of interest [*Pseudomonas syringae* (PS)]. The LSS operates on the same principles as those associated with standard, nanoaerosol condensation particle counter (CPC) (Balendra et al. 2024; Deng et al. 2024). The initial SWV data as profiled in Fig. F1 suggest an increased presence of *PS* on 29 and 30 July as compared to the other days. It is noted that this is the very first deployment of CINCS, and to evaluate actual quantities of *PS*, a controlled calibration series (say with FM120) is necessary, which was not possible in time for Fatima-GB due to scheduling conflicts.

(ii) The MBS deployed by UMAN detects primary bioaerosols and fluorescent aerosols in real time via the interrogation of single-particle autofluorescence and morphology. The MBS excites a single particle with a 280-nm filtered xenon flashlamp and detects resultant fluorescent emissions over eight channels between 305 and 655 nm. Particle size is resolved via Mie scattering of a 635-nm laser (detection range of 0.5–15 μm in diameter), and particle morphology is approximated via the recording of two parallel chords of the 2D scattering pattern with a dual complementary metal-oxide semiconductor (CMOS) array; for a full description, see Crawford et al. (2023). Classification of particles into representative groups of interest was accomplished using the single-particle fluorescent spectra, following Freitas et al. (2022). First, 3-sigma and 9-sigma thresholding is conducted simultaneously to retain weakly fluorescent populations of interest (e.g., sea spray with organic content), clipping all negative values in each channel at 0 after threshold subtraction (Crawford et al. 2020). FSSAs are defined as those which exceed the 3-sigma threshold but not the 9-sigma threshold; HFSSA exceeds the 9-sigma threshold where the maximum intensity is not observed in the second channel; and PBAP exceeds the 9-sigma threshold with the maximum intensity observed in the second channel. Particles which do not exceed the 3-sigma threshold are classified as nonfluorescent. A time series of the different classes is then produced using a 5-min integration period, which is shown in Figs. F2a and F2b.

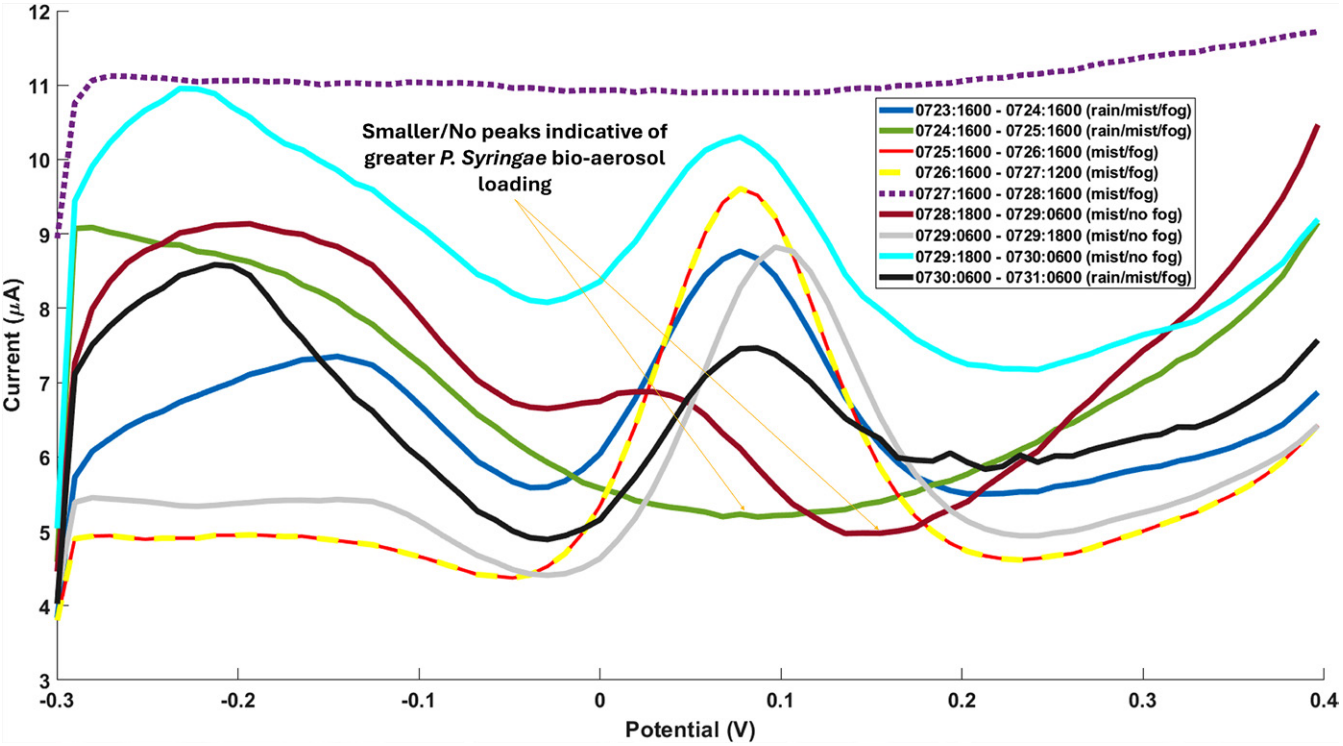

Fig. F1. Initial SWV results. Decreased and/or no peaks in the output current suggest an increased proportion and loading of *PS* in the SI ambient air. Note smaller peaks (greater PS) on 29 and 30 Jul, indicating a possible association of rain with the *PS* population. Note that during 0727:1600 and 0728:1800 plots represent periods that SWV failed and hence anomalous SWV tests (time is in ADT).

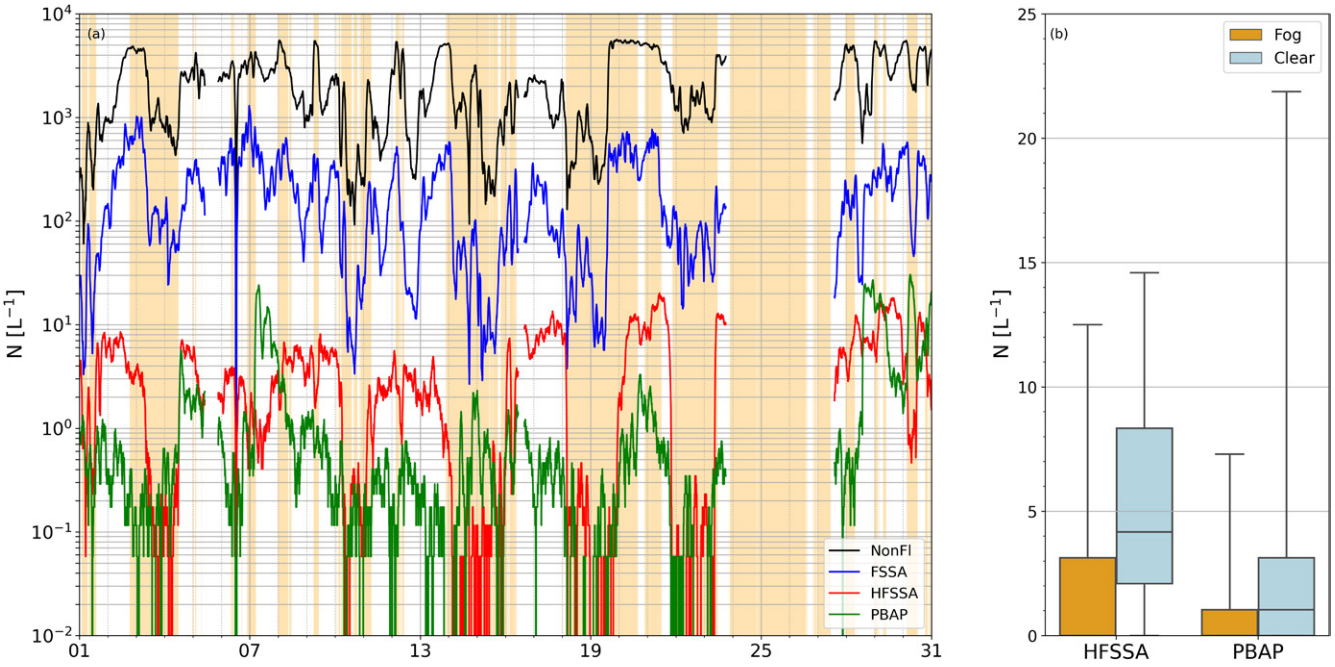

Fig. F2. (a) MBS aerosol concentrations *N* from 1 to 31 Jul based on the above characterization. A 3-hourly rolling average has been applied to the 5-min integrated time series for clarity. Shading shows fog periods identified by (1-min averaged) visibility <1 km. (b) A box-and-whisker plot showing the impact of fog on the HFSSA and PBAP classes. Whiskers denote the 5th and 95th percentiles.

Appendix G
Homogeneity of Fog Across SI and Monitoring Droplet Evolution

Useful microphysical and visibility data that supplement meteorological information in Fig. 9 pertinent to a cloud-lowering fog event are given in Fig. G1.

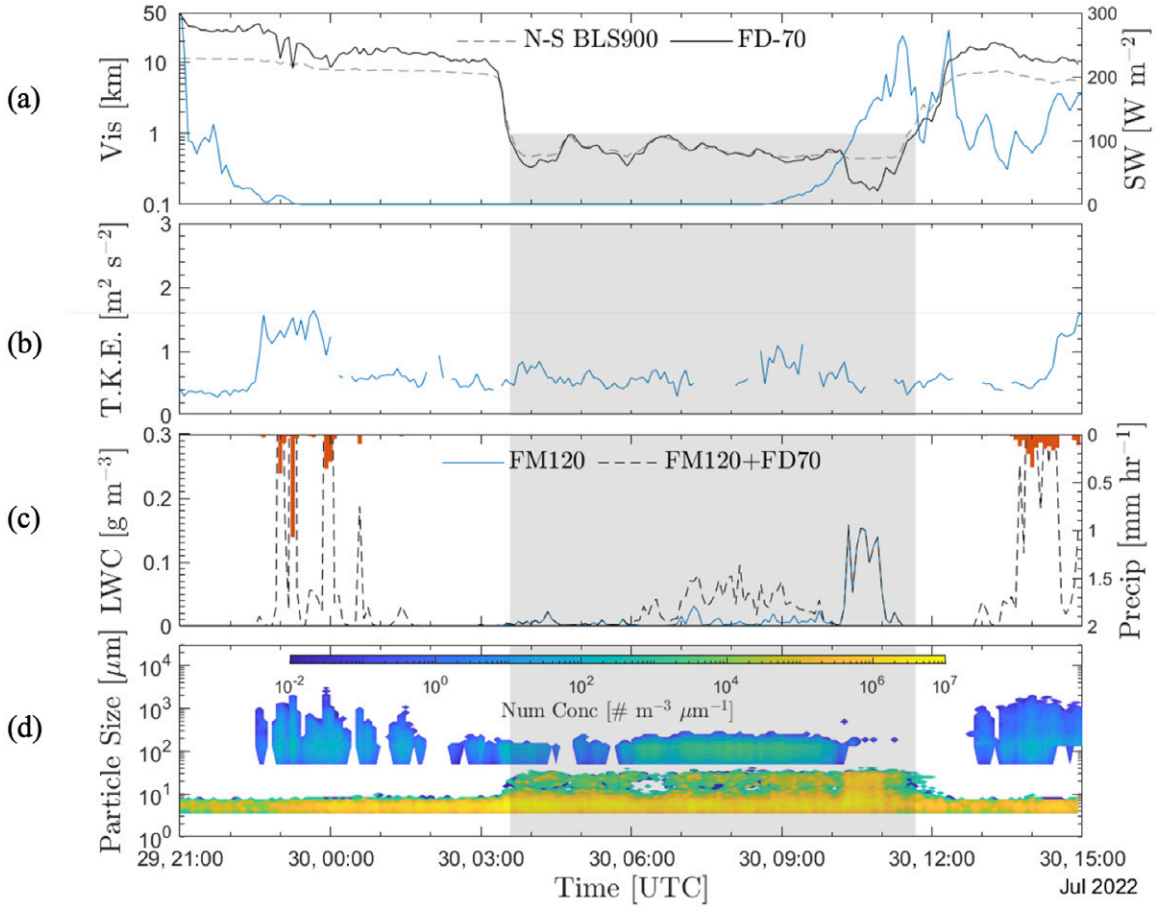

Fig. G1. (a) Time series of visibility from FD70 and BLS900 scintillometer along with net SWR (blue). SWR and FD70 were both near the center tower, while the scintillometer gave a spatially integrated measurement from the north tower to the south tower. Thus, a disparity between FD70 and BLS900 indicates hydrometeor inhomogeneities. (b) Time series of TKE from the 8-m level at the center tower. (c) LWC calculated from FM120 as well as the combined LWC from the FM120 and FD70. Red indicates precipitation from FD70. (d) Time series of droplet size distribution from FD70 and FM120. Gray highlighted area denotes persistent fog. Note that the number concentration from FD70 is only an estimate, which should be viewed with circumspection along with the corresponding LWC retrievals.

Appendix H
A Brief Overview of COAMPS Modeling

Coupled Ocean Atmosphere Mesoscale Prediction System (COAMPS) was used in real time to support Fatima-GB, wherein 48-h forecasts were launched four times a day at 0000, 0600, 1200, and 1800 UTC. The numerical setup for Sable Island utilized three nested domains with decreasing horizontal grid spacing from 9 to 1 km, as shown in Fig. H1. In the vertical direction, there were 23 model levels in the lowest 1 km, starting at 3 m close to the surface and then increasing with height, for a total of 68 layers with the model top at 28 km. The time step for the coarsest mesh was 30 s. The grids encompassing the position of R/V *Condor* were also evaluated.

COAMPS is a fully compressible, nonhydrostatic limited-area model developed and used operationally by the U.S. Navy (Hodur 1997). The initial and lateral boundary conditions for COAMPS were provided using GFS fields. The sea surface temperature gradient between the

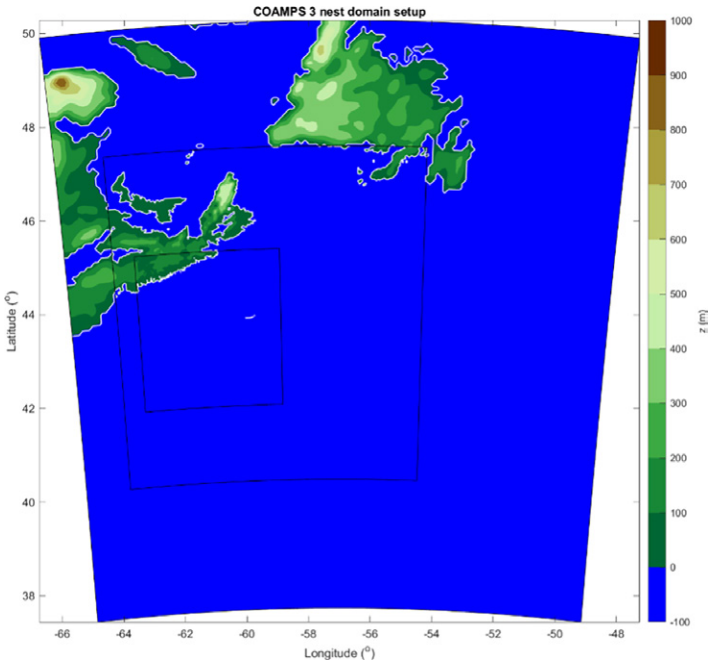

Fig. H1. COAMPS nests (9, 3, and 1 km) over the northwestern Atlantic, centered over SI, used for the real-time support of Fatima-GB.

Labrador Current and Gulf Stream that plays an important role in the fog life cycle is relatively stationary during each forecast (not shown), justifying not coupling the ocean component in COAMPS. The SST was captured by the data assimilation cycle and provided as the bottom boundary condition for the atmospheric component of COAMPS.

Appendix I
Satellite Evidence of Fog Shadow

Brightness temperature difference (BTD) fields observed by specific wavelength channels of satellites can be used to roughly identify smaller water droplets (and hence fog or stratus) in the lower atmosphere (Amani et al. 2020). This property was exploited to identify Sable Island's fog shadow in the images of the *GOES-18* satellite shown in Fig. I1. Fog shadow extends well beyond the spatial resolution limits of *GOES-18*.

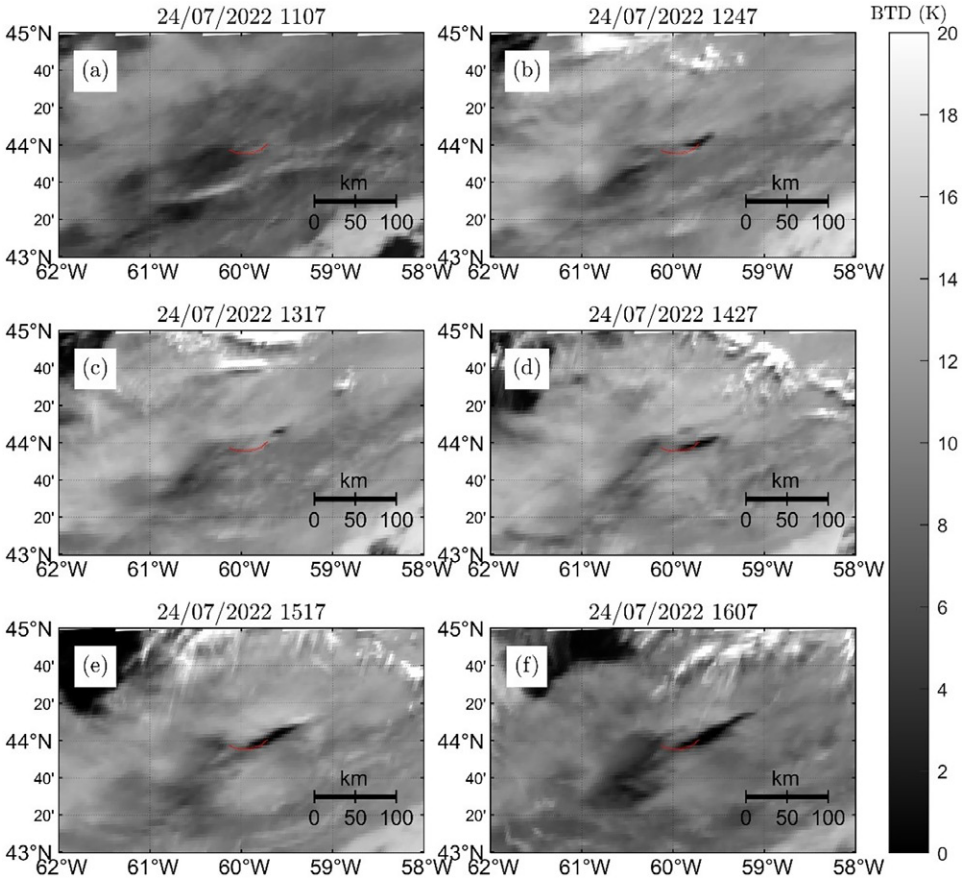

Fig. I1. BTD calculated based on (10.35–3.9 μm) wavelength channels of the *GOES-18* satellite observed in the vicinity of Sable on 24 Jul 2022 (IOP10) at different observation times; see Bardoel et al. (2025). The times of images are shown on the top in ADT. A region of improved visibility appears after 1200 ADT on 24 Jul (dark region) in the lee (NE) of Sable that persists, with varying intensities, at least until 1600 ADT. The dark region that extends ~30 km downstream can be construed as the fog shadow predicted by COAMPS.

Appendix J
Simulating Fog Dynamics via Coupled Modeling

LES resolves turbulent eddies down to the scale of grid size and provides insights into much smaller microscale conditions that govern the life cycle of fog. Following Fatima-GB, LES coupled with LSD and LCM models (dubbed L^3) helped understand and predict the microscale dynamics of fog. The L^3 solves the following governing equations numerically using a finite-difference spatial discretization and second-order time integration. The role of each term is identified beneath the curly brackets:

$$\frac{\partial \tilde{u}_i}{\partial t} = \underbrace{-\tilde{u}_j \frac{\partial \tilde{u}_i}{\partial x_j}}_{\text{resolved}} \underbrace{-\frac{1}{\rho_0}\frac{\partial \tilde{p}}{\partial x_i}}_{\text{pressure}} \underbrace{-\frac{\partial \tau_{ij}}{\partial x_j}}_{\text{subgrid}} + \underbrace{\delta_{i,3}\frac{\tilde{\theta}_v - \tilde{\theta}_v}{\tilde{\theta}_v}}_{\text{buoyancy}} + \underbrace{\varepsilon_{ij3} f\left(\tilde{u}_j - u_{g,j}{}^{\text{LS}}\right)}_{\text{Coriolis}} \underbrace{-u_j{}^{\text{LS}}\frac{\partial u_i{}^{\text{LS}}}{\partial x_j}}_{\text{LS advection}} \\ \underbrace{-w^{\text{LS}}\frac{\partial \tilde{u}_i}{\partial z}}_{\text{LS subsidence}} \underbrace{+\frac{1}{\tau_n}\left(u_i^{\text{LS}} - \tilde{u}_i\right)}_{\text{relaxation}} \underbrace{+\frac{1}{\rho_a}S^m}_{\text{source}}, \tag{J1}$$

$$\frac{\partial \tilde{\phi}}{\partial t} = \underbrace{-\tilde{u}_j \frac{\partial \tilde{\phi}}{\partial x_j}}_{\text{resolved}} \underbrace{-\frac{\partial \pi_j}{\partial x_j}}_{\text{subgrid}} \underbrace{-u_j{}^{\text{LS}}\frac{\partial \phi^{\text{LS}}}{\partial x_j}}_{\text{LS advection}} \underbrace{-w^{\text{LS}}\frac{\partial \tilde{\phi}}{\partial z}}_{\text{LS subsidence}} \underbrace{+\frac{1}{\tau_n}\left(\phi^{\text{LS}} - \tilde{\phi}\right)}_{\text{relaxation}} \underbrace{+\frac{1}{\rho_a}S^h}_{\text{source}}. \tag{J2}$$

Here, $\tilde{u}_i$ is the filtered velocity and θ_v is the virtual potential temperature. The term $\tilde{\phi}$ is a generic scalar, which can be either the potential temperature $(\tilde{\theta})$ or the total specific humidity $\tilde{q}$. The large-scale advective tendencies and subsidence and the Coriolis term that accounts for the large-scale pressure gradients are the LSD terms. A relaxation term is introduced as a safeguard, nudging the LES toward a true mean state. A dynamic subgrid-scale (SGS) model developed by Germano et al. (1991) is used for modeling SGS stresses. The LCM model addresses the interaction between fog droplets and the background flow, providing a detailed representation of fog formation and growth processes.

The size of the computational domain used to simulate the Hibernia area, a locality covered by R/V *Condor*, is 500 m × 500 m × 500 m in the *x*, *y*, and *z* (upward) directions, respectively. This domain is divided into 128 × 128 × 128 grid points with 3.9-m grid spacing in each direction. Periodic boundary conditions are applied horizontally, while at the bottom surface, the Monin–Obukhov similarity theory defines surface conditions with a roughness length of 3.2×10^{-5} m. The ocean surface is forced by SST derived from ERA5, updated hourly, and specific humidity is adjusted to maintain 100% relative humidity at the surface. The large-scale tendencies are derived from ERA5 and interpolated on the LES grid. The relaxation time is set to 1 h. For the LCM, the initial aerosol distribution is based on the C-FOG campaign data (Fernando et al. 2021) and includes accumulation and coarse modes with peaks at 0.1 and 1 μm with hygroscopicities of 0.6 and 1.2, respectively.

Appendix K
Instrumentation for Fatima-GB

Instruments (Table K1) and instrument systems (Table K3) on Atlantic *Condor* and instruments on Sable Island (Table K2) are given below.

Table K1. Instrumentation on R/V *Atlantic Condor*.

Instrument	Manufacturer and model	Measurement	Location	Institution
MRR	METEK MRR-PRO	Vertical profiling of droplet size distribution, rain rate, and liquid water content	On ship	UND
VMP	Rockland Scientific Uprising VMP-250	Ocean microstructure, TKE dissipation evaluation	On ship	UND
Optical disdrometer	Eigenbrodt ODM 470	Raindrop or snow particle size distribution	On ship	UND
ROSR	Remote Measurements and Research Co.	Sea surface skin temperature (SSST)	On ship	UND
MWR	Radiometrics MP-3000A	Vertical profile of temperature, water vapor, and liquid water	On ship	UND
Visible and cloud/ IR cameras	Moonglow Technologies Sky Camera; FLIR DUO Pro R IR Thermal Camera	Full-color video view of the entire sky; real-time image capture plus MSX multispectral imaging enhancement	On ship	UND
Visibility and PWD sensor	Vaisala FD70	Meteorological condition code and MOR (visibility), raindrop or snow particle size distribution	On ship	UND
Ceilometer CL61	Vaisala CL61	Vertical profiles of aerosol backscatter with depolarization; precipitation, differentiation between solid, liquid, and mixed-phase clouds	On ship	UND
Scanning Doppler lidar	Halo Photonics Streamline Allsky	Profiles of Doppler velocity and fluctuations, aerosol backscatter	Motion-stabilized platform	UND
W-band FMCW cloud radar	Radiometric Physics RPG-FMCW-94-DP-G1	Vertical profiles of reflectivity, Doppler velocity, 2.2-mm wavelength, range resolution of 1 m, information of scatterers (rain, clouds, snowflakes, fog)	Motion-stabilized platform	UND
CTD	Sea-Bird SBE 25plus	Conductivity–temperature–depth sensors, and auxiliary sensors—dissolved oxygen, pH, fluorescence, oil, radiance, light transmission, turbidity, nitrates	On ship	UND/MEOPAR
300-kHz ADCP	Teledyne Workhorse	Ship mounted, bottom-referenced velocity, and current profile measurement	On ship	UND/MEOPAR
Sea snake	Built by NOAA (YSI 46040 precision thermistor in a custom-fabricated floating hose)	Sea surface temperature at ~3–5 cm below sea surface	On ship	UND/PSL-NOAA
3D ultrasonic anemometer	Gill R3A	3D wind velocity (@20 Hz at 18.6 m above the surface	(Ship) Bowmast	PSL-NOAA/UND
Fast water vapor infrared gas analyzer	LI-COR 7500A	Water vapor (@10 Hz) at 18 m above the surface	Bowmast	PSL-NOAA/UND
Weather TX	Vaisala WXT520	Temperature, RH, pressure, rain, and WS/ direction (@1 Hz) at 18 m above the surface	Bowmast	PSL-NOAA/UND
GPS heading system	Hemisphere Crescent VS100	GPS coordinates	Bowmast	PSL-NOAA/UND
HMP pressure sensor	Vaisala	Pressure at 16.25 m above the surface	Bowmast	PSL-NOAA/UND
Pyrgeometers	Eppley PIR	Downwelling LW radiative flux (on the bridge at ~16–17 m height)	Bowmast	PSL-NOAA/UND
Pyrometers	Kipp and Zonen CM22 and CMP22	Downwelling SW radiative flux (on the bridge at ~16–17 m height)	Bowmast	PSL-NOAA/UND
Moored wave buoy	Sofar Ocean, Spotter	Ocean wave directional spectra and bulk wave statistics (significant wave height, direction, period), bulk water temperature	3 km south of SI	NPS
Rawinsonde (Vaisala MW41)	Vaisala DigiCORA MW41 Sounding System	Upper air soundings of temperature, RH, pressure, WS, and WD	Off ship	NPS

(*Continued*)

Table K1. (*Continued*).

Instrument	Manufacturer and model	Measurement	Location	Institution
Ocean surface and scene visualization cameras	1x Campbell Scientific Field Camera, 2x InVid Technology Bullet Cameras	Optical/infrared images (full motion video and stills)	On ship	NPS
Integrated CO_2 and H_2O open-path gas analyzer and 3D Sonic wind anemometer	Campbell Scientific IRGASON	Perturbation of three-dimensional wind vector, sonic air temperature, H_2O/CO_2 gas concentration	C-CAMS and D-CAMS	NPS
Dual-antenna GNSS-aided inertial navigation system	VectorNav VN-300	Platform motion (GNSS position, velocity, attitude)	C-CAMS and D-CAMS	
Humidity and temperature probe	Vaisala HMP155	Bulk temperature and RH	C-CAMS and D-CAMS	NPS
Fast-response barometer	Paroscientific MET4A	Pressure perturbation w/aspirated temperature and RH	C-CAMS	NPS
Upwelling infrared pyrometer	Heitronics CT15.85	Radiometric sea surface temperature (9.6–11.6 μm)	C-CAMS and D-CAMS	NPS
Net radiometer	Apogee SN-500-SS	Net LW and SW radiation	C-CAMS	NPS
Radar altimeter	Ainstein U.S.-D1	Surface elevation	C-CAMS	NPS
Soot photometer	Brechtel Tricolor Absorption Photometer (TAP)	Aerosol absorption (red, green, blue)	C-CAMS	NPS
Portable optical particle spectrometer	Handix Scientific POPS	Aerosol size spectra (120 nm–3 μm)	C-CAMS	NPS
Visibility and PWD sensor	Campbell Scientific CS-125	Infrared forward-scattering MOR (visibility)	C-CAMS and D-CAMS	NPS
Fog monitor	Droplet Measurement Technologies FM120	Droplet size spectra (2–50 microns)	C-CAMS and D-CAMS	NPS
3-wavelength integrating nephelometer	Ecotech Aurora 3000	Aerosol scattering (red, green, blue)	On ship	AFIT/NPS
Black carbon aethalometer	Magee Scientific AE33	Aerosol absorption (7 wavelength, UV-NIR)	On ship	AFIT/NPS
(Water-based) CPC	Aerosol devices MAGIC210 CPC	Aerosol number concentration (5 nm–2.5 μm), moderated aerosol growth with internal water cycling, CPC	On ship	AFIT/NPS
Pyrgeometer	Apogee SL-510, SL-610	LW down- and upwelling radiation	TLS mounted on ship	UU
OPC	AlphaSense OPC-N3 model	PM1, PM2.5, PM10, and particle size distribution (0.35 to 40 μm with 24 bins	TLS mounted on ship	UU
Fog water collector	Caltech Active Strand Cloud Water Collector 2	Droplets > 3.5 μm	On ship	DU
SMPS	TSI Inc. 3938 differential-mobility analyzer 3081 + electrostatic classifier 3082 + CPC 3772	Submicrometer particle size distribution: aerosol size spectra 10–500 nm	On ship	DU
APS	TSI Inc. 3321	Aerosol size spectra (0.36–13 μm)	On ship	DU
Fog monitor	DMT FM120	Droplet size spectra (2–50 μm)	On ship	DU
Backscatter cloud probe	DMT BCP	Particle size distribution (5–75 μm)	Gondola	OntTechU
CDP	DMT CDP-2	Particle size distribution (2–50 μm)	Gondola	OntTechU

(*Continued*)

Table K1. (*Continued*).

Instrument	Manufacturer and model	Measurement	Location	Institution
MOUDI	Model 100-NR, MSP Corp (A TSI Company), Shoreview, Minnesota	0.1–10 μm, aerosol during fog	On ship	YorkU
Nano-MOUDI-II	Model 122-R, MSP Corp (TSI)	0.01–10 μm, ambient aerosol	On ship	YorkU
Ion chromatograph	Thermo Scientific ICS-6000	Aerosol major anions and cations	On ship	YorkU
Gas monitors	Ecotech EC9841, EC9830, S10, S40	CO, NO, NO_2, total reactive nitrogen, NH_3, and O_3	On ship	YorkU
Fog monitor	DMT FM-120	Droplet size spectra (2–50 μm)	A/V Wallace	Scripps/UCSD
Flux mast (Sonics)	Gill R3-50 (×2)	3D WS and fluxes	A/V Wallace	Scripps/UCSD
Towed CTD	RBR Concerto	Ibid, dissolved oxygen, fluorometer	A/V Wallace	Scripps/UCSD
500-Hz ADCP (downward looking)	Nortek Signature 500	Current profiler	A/V Wallace	Scripps/UCSD
Visible and IR 360 camera	ASV	Surface IR and visible imagery	A/V Wallace	Scripps/UCSD
X-band radar	Furuno	X-band backscatter	A/V Wallace	Scripps/UCSD
3D ultrasonic anemometer	Gill R3-50	3D winds and fluxes	Wave gliders (×3)	Scripps/UCSD
Weather station	Vaisala WXT530	Temperature, RH, pressure, rain, and WS/direction (@1 Hz)	Wave gliders (×3)	Scripps/UCSD
CTD	Sea-Bird GPCTD	Ibid, at the surface and subdepth (~8–9 m)	Wave gliders (×3)	Scripps/UCSD
300-KHz ADCP	Teledyne Workhorse	Ibid, current profile	Wave gliders (×3)	Scripps/UCSD
Upward-looking current profiler	Nortek Signature 1000	Upward-looking current profiler at 8-m depth	Wave gliders (×3)	Scripps/UCSD
Dual-GPS RX	Hemisphere V104	Position, platform velocity, and directional wave spectra	Wave gliders (×3)	Scripps/UCSD
CTD	RBR Concerto installed on profiling Winch	Ibid, profiling from 8- to 150-m depth (installed on only one wave glider)	Wave gliders (×3)	Scripps/UCSD
GPS-IMU	Novatel SPAN OEM7720 GPS RX with dual-GPS antennas and Epson EG320N IMU	Position, platform attitude and velocity, directional wave spectra	Wave gliders (×3)	Scripps/UCSD

Table K2. Instrumentation on Sable Island.

Instrument	Manufacturer and model	Measurement	Institution
Visibility and PWD sensor	Vaisala FD70	Ibid	UND
Visibility and PWD sensor	Vaisala PWD22	Meteorological condition code and meteorological optical range (MOR) (or visibility)	UND
Scanning Doppler lidar	Halo Photonics Streamline Allsky	Ibid	UND
Super Combo probe	In-house built (miscellany of hot-wire and nanowire sensors aligning with the wind to capture dissipation scales)	High-frequency measurement of wind velocity and temperature fluctuations with resolution approaching dissipation scales	UND
Net radiometers	Campbell Scientific CNR1 net radiometer	Net LW/SW radiation	UND
Fast water vapor infrared gas analyzer	LI-COR LI-7500A	Ibid	UND
Sonic anemometers	Gill R3A	Ibid	UND
Fine-wire *T*/relative humidity sensors	Vaisala HMP45C	Temperature and RH	UND

(*Continued*)

Table K2. (*Continued*).

Instrument	Manufacturer and model	Measurement	Institution
Ceilometer CL31	Vaisala CL31	Vertical profiles of aerosol backscatter	UND
MWR	Radiometrics MP-3000A	Ibid	NPS
Wind profiling monostatic Sodar	Scintec SFAS	Vertical profiles of WS/direction and structure function parameter of temperature (10–500 m)	NPS
Scintillometer	Scintec BLS 900	Fried parameter *r*0, structure function parameter of index of refraction Cn2	NPS
Differential imaging motion monitor	NAWCWD China Lake—DIMM	Fried parameter *r*0, structure function parameter of index of refraction Cn2	NPS
Wide-angle teleradiometric transmissometer	NAWCWD China Lake—WATT	Optical transmission	NPS
Noncoherent extended source Beacon	NAWCWD China Lake—NESB	SW IR TX for DIMM/WATT systems	NPS
Rawinsonde (Vaisala MW41)	Vaisala DigiCORA MW41 Sounding System	Upper air soundings of temperature, RH, pressure, WS, and WD	NPS
TLS; balloon and winch	Allsopp Helikite DS25	Lifting meteorological payload to various elevations	NPS
Visibility and present weather sensor	Campbell Scientific CS-120	Infrared forward-scattering MOR (visibility)	NPS
CDP on communication tower	DMT CDP-2	Ibid	NPS
Transmissometer	Vaisala LT31	Optical transmission	NPS
DTS	Omega Type-E Thermocouple	Structure function parameter of temperature (CT2) from three unequally spaced fast-response thermocouples	NPS
Integrated CO_2 and H_2O open-path gas analyzer and 3D Sonic wind anemometer	Campbell Scientific IRGASON	Ibid	NPS
Video cameras	Axis Communications M30 Dome Camera	Visual documentation of environmental conditions	NPS
MRR	METEK MRR-PRO	Ibid	UU
Ceilometer CL31	Vaisala CL31	Ibid	UU
EM scintillometer (TX and RX)	Scintec BLS-900#1TX, BLS-900#1RX	Atmospheric turbulence, heat flux, and crosswind	UU
Microwave scintillometer (MWS)	Radiometer Physics RPG-MWSC-160 (TX and RX)	Sensible and latent heat fluxes	UU
Precision radiation balance sawhorse	CGR4 pyrgeometers, CMP21 pyranometers, up- and downwelling; in-house built	Four components of SW, LW, and net radiation	UU
Pyrgeometer (on TLS)	Apogee SL-510, SL-610	LW down- and upwelling radiation	UU
OPC	AlphaSense OPC	PM1, PM2.5, PM10, and particle size distribution (0.35–40 μm with 24 bins N3)	UU
Visibility cameras (webcams)	Microseven 5MP	Time-lapse photos (1 per minute)	UU
LWC probes	In-house built	Liquid water content	UU
Self-calibrating soil heat flux sensor	Hukseflux HFP01SC	Soil heat flux	UU
30-cm soil moisture and temperature sensor	Campbell Scientific CS650	Soil moisture and temperature	UU
Averaging soil thermocouple probe	Campbell Scientific TCAV	Soil temperature	UU
Visibility and present weather sensor	Campbell Scientific CS125	Infrared forward-scattering MOR (visibility)	UU
LEMS (automated weather station)	In-house assembled	*T*, RH, WS and direction, soil *T*, surface *T*, SW, and OPC-N3 (0.38–17 μm with 24 bins)	UU

(*Continued*)

Table K2. (*Continued*).

Instrument	Manufacturer and model	Measurement	Institution
Ceilometer	Vaisala CL51	Vertical profiles of aerosol backscatter	OntTechU
Weather TX	Vaisala WXT520	Ibid	OntTechU
Visibility and PWD sensor	Vaisala PWD52	Meteorological condition code and MOR (visibility) and rain	OntTechU
Fog monitor	DMT FM120	Ibid	OntTechU
GCIP	DMT	Particle size spectra (7.5–960 μm)	OntTechU
Young 3D Sonic anemometer (Model 81000)	R.M. Young Company	Horizontal and vertical WS and direction and turbulence, 20 Hz	OntTechU
Sunshine pyranometer	Delta-T Devices SPN1	Global (total) and diffuse irradiance; direct normal irradiance (DNI) calculation	OntTechU
Digital camera	General	Local pictures looking at the south	OntTechU
CINCS	Aerosol Devices, Inc.	Bioaerosols tens of nanometer, possibly of fog/ice condensation nucleus nature	AFIT/NPS
MBS-MR	University of Hertfordshire	Ultraviolet light-induced fluorescence spectrometer; primary bioaerosol particles, detection range of 0.5–15 μm	UMAN

Table K3. Instrument systems on R/V *Atlantic Condor*.

System	Location	Institution
Bowmast	Ship bow	PSL-NOAA/UND
C-CAMS	Crane operated (ship)	NPS
D-CAMS	Deck mounted on ship	NPS
TLS + payload	Ship and SI	ARL/UU/UND
Gondola	Ship (fixed)	OntTechU
Instrument wave glider	Launched from ship	SCRIPPS/UCSD
A/V *Wallace*: autonomous boat instrumented for air–sea interaction research	Launched from ship	SCRIPPS/UCSD
Flux towers (appendix C)	SI	UND/UU
LEMS	SI	UU
Motion-stabilized Doppler lidar	Ship	UND
Motion-stabilized W-band radar	Ship	UND
Super Combo probe	SI	UND
Radiation balance sawhorse	SI	UU
Instrumented UAV	SI/2 weeks	OntTechU
Microphysical tower	SI	OntTechU

Appendix L
Commonly Encountered Acronyms

For acronyms for instruments, see appendix K.

ABL	Atmospheric boundary layer
AGL	Above ground level
MSL	Above mean sea level
BTD	Brightness temperature difference
COAMPS	Coupled Ocean–Atmosphere Mesoscale Prediction System
CTD	Conductivity–temperature–depth
DWR	Downwelling radiation (irradiance)
ERA5	Fifth major global reanalysis produced by ECMWF
FCN	Fog condensation nuclei
FSSA	Fluorescent sea spray aerosols
GFS	Global Forecast System
HFSSA	Highly fluorescent sea spray aerosols
IBL	Internal boundary layer
IOP/ISP	Intense operational period/intense study period
K	Kolmogorov
L3	Coupling of LES, LSD, and LCM
LCM	Lagrangian cloud model
LES	Large-eddy simulation
LSD	Large-scale dynamics
LEMS	Local energy budget measurement system
LWC	Liquid water content
LWR	Longwave radiation
MABL	Marine atmospheric boundary layer
MSLP	Measured sea level pressure
MVD	Mean volume diameter
NWP	Numerical weather prediction
Nd	Aerosol number concentration
O–C	Obukhov–Corrsin
PBAP	Primary biological aerosol particles
RH	Relative humidity
SLOP	Sable Lee Observing Period
SSA	Sea surface aerosol
SST	Sea surface temperature
SWR	Shortwave radiation (irradiance)
T	Temperature
TKE	Turbulent kinetic energy
WRF (ARW)	Weather Research and Forecasting Model (Advanced Research version of WRF)
WS and WD	Wind speed and wind direction

References

Amani, M., S. Mahdavi, T. Bullock, and S. Beale, 2020: Automatic nighttime sea fog detection using GOES-16 imagery. *Atmos. Res.*, **238**, 104712, https://doi.org/10.1016/j.atmosres.2019.104712.

Balendra, S., A. Kale, J. Pongetti, M. Kazemimanesh, M. Haugen, L. Weller, and A. Boies, 2024: Condensation particle counters: Exploring the limits of miniaturisation. *J. Aerosol Sci.*, **175**, 106266, https://doi.org/10.1016/j.jaerosci.2023.106266.

Bardoel, S., and Coauthors, 2025: Study of fog dissipation in an internal boundary layer on Sable Island. *Quart. J. Roy. Meteor. Soc.*, **151**, e4891, https://doi.org/10.1002/qj.4891.

Barve, A., I. Gultepe, H. J. S. Fernando, Q. Wang, and L. Shen, 2025: Large scale dynamics large-eddy simulation Lagrangian Clous Modeling (L3) coupling for studying the marine fog life cycle. *Quart. J. Roy. Meteor. Soc.*, in press.

Bertram, T. H., R. E. Cochran, V. H. Grassian, and E. A. Stone, 2018: Sea spray aerosol chemical composition: Elemental and molecular mimics for laboratory studies of heterogeneous and multiphase reactions. *Chem. Soc. Rev.*, **47**, 2374–2400, https://doi.org/10.1039/C7CS00008A.

Bhushan, B., 2020: Design of water harvesting towers and projections for water collection from fog and condensation. *Philos. Trans. Roy. Soc.*, **A378**, 20190440, https://doi.org/10.1098/rsta.2019.0440.

Boutle, I., J. Price, I. Kudzotsa, H. Kokkola, and S. Romakkaniemi, 2018: Aerosol–fog interaction and the transition to well-mixed radiation fog. *Atmos. Chem. Phys.*, **18**, 7827–7840, https://doi.org/10.5194/acp-18-7827-2018.

Chen, F., and J. Dudhia, 2001: Coupling an advanced land surface–hydrology model with the Penn State–NCAR MM5 modeling system. Part I: Model implementation and sensitivity. *Mon. Wea. Rev.*, **129**, 569–585, https://doi.org/10.1175/1520-0493(2001)129<0569:CAALSH>2.0.CO;2.

Chisholm, N., and Coauthors, 2021: Characterizing atmospheric aerosols off the Atlantic Canadian Coast during C-FOG. *Bound.-Layer Meteor.*, **181**, 345–364, https://doi.org/10.1007/s10546-021-00673-7.

Crawford, I., D. Topping, M. Gallagher, E. Forde, J. R. Lloyd, V. Foot, C. Stopford, and P. Kaye, 2020: Detection of airborne biological particles in indoor air using a real-time advanced morphological parameter UV-LIF spectrometer and gradient boosting ensemble decision tree classifiers. *Atmosphere*, **11**, 1039, https://doi.org/10.3390/atmos11101039.

——, K. Bower, D. Topping, S. Di Piazza, D. Massabò, V. Vernocchi, and M. Gallagher, 2023: Towards a UK Airborne Bioaerosol Climatology: Real-time monitoring strategies for high time resolution bioaerosol classification and quantification. *Atmosphere*, **14**, 1214, https://doi.org/10.3390/atmos14081214.

Crilley, L. R., M. Lao, L. Salehpoor, and T. C. VandenBoer, 2023: Emerging investigator series: An instrument to measure and speciate the total reactive nitrogen budget indoors: Description and field measurements. *Environ. Sci.: Processes Impacts*, **25**, 389–404, https://doi.org/10.1039/D2EM00446A.

Deng, Z., and Coauthors, 2024: Size-resolved cloud condensation nuclei activity of aerosol particles sampled above the mixing layer. Aerosol Sci. Technol., **58**, 485–497, https://doi.org/10.1080/02786826.2024.2330475.

Dimitrova, R., A. Sharma, H. J. S. Fernando, I. Gultepe, V. Danchovski, S. Wagh, S. L. Bardoel, and S. Wang, 2021: Simulations of coastal fog in the Canadian Atlantic with the Weather Research and Forecasting Model. *Bound.-Layer Meteor.*, **181**, 443–472, https://doi.org/10.1007/s10546-021-00662-w.

Dorman, C. E., J. Mejia, D. Koračin, and D. McEvoy, 2017: Worldwide marine fog occurrence and climatology. *Marine Fog: Challenges and Advancements in Observations, Modeling, and Forecasting*, Springer, 7–152.

——, ——, ——, and ——, 2020: World marine fog analysis based on 58-years of ship observations. *Int. J. Climatol.*, **40**, 145–168, https://doi.org/10.1002/joc.6200.

Dudhia, J., 1989: Numerical study of convection observed during the Winter Monsoon Experiment using a mesoscale two-dimensional model. *J. Atmos. Sci.*, **46**, 3077–3107, https://doi.org/10.1175/1520-0469(1989)046<3077:NSOCOD>2.0.CO;2.

Fairall, C. W., E. F. Bradley, J. E. Hare, A. A. Grachev, and J. B. Edson, 2003: Bulk parameterization of air-sea fluxes: Updates and verification for the COARE algorithm. *J. Climate*, **16**, 571–591, https://doi.org/10.1175/1520-0442(2003)016<0571:BPOASF>2.0.CO;2.

Farmer, D. K., E. K. Boedicker, and H. M. DeBolt, 2021: Dry deposition of atmospheric aerosols: Approaches, observations, and mechanisms. *Annu. Rev. Phys. Chem.*, **72**, 375–397, https://doi.org/10.1146/annurev-physchem-090519-034936.

Fathalli, M., C. Lac, F. Burnet, and B. Vié, 2022: Formation of fog due to stratus lowering: An observational and modelling case study. *Quart. J. Roy. Meteor. Soc.*, **148**, 2299–2324, https://doi.org/10.1002/qj.4304.

Fernando, H. J. S., and Coauthors, 2021: C-FOG: Life of coastal fog. *Bull. Amer. Meteor. Soc.*, **102**, E244–E272, https://doi.org/10.1175/BAMS-D-19-0070.1.

Freitas, G. P., C. Stolle, P. H. Kaye, W. Stanley, D. P. R. Herlemann, M. E. Salter, and P. Zieger, 2022: Emission of primary bioaerosol particles from Baltic seawater. *Environ. Sci. Atmos.*, **2**, 1170–1182, https://doi.org/10.1039/D2EA00047D.

Gautam, R., and M. K. Singh, 2018: Urban heat island over Delhi punches holes in widespread fog in the Indo-Gangetic Plains. *Geophys. Res. Lett.*, **45**, 1114–1121, https://doi.org/10.1002/2017GL076794.

Ge, X., Q. Zhang, Y. Sun, C. R. Ruehl, and A. Setyan, 2012: Effect of aqueous-phase processing on aerosol chemistry and size distributions in Fresno, California, during wintertime. *Environ. Chem.*, **9**, 221–235, https://doi.org/10.1071/EN11168.

Gerber, H. E., 1981: Microstructure of a radiation fog. *J. Atmos. Sci.*, **38**, 454–458, https://doi.org/10.1175/1520-0469(1981)038<0454:MOARF>2.0.CO;2.

Germano, M., U. Piomelli, P. Moin, and W. H. Cabot, 1991: A dynamic subgrid-scale eddy viscosity model. *Phys. Fluids*, **3**, 1760–1765, https://doi.org/10.1063/1.857955.

Goldschmidt, V. W., and M. K. Householder, 1969: The hot wire anemometer as an aerosol droplet size sampler. *Atmos. Environ.*, **3**, 643–651, https://doi.org/10.1016/0004-6981(69)90021-3.

Grare, L., N. M. Statom, N. Pizzo, and L. Lenain, 2021: Instrumented wave gliders for air-sea interaction and upper ocean research. *Front. Mar. Sci.*, **8**, 664728, https://doi.org/10.3389/fmars.2021.664728.

Greenfield, S. M., 1957: Rain scavenging of radioactive particulate matter from the atmosphere. *J. Meteor.*, **14**, 115–125, https://doi.org/10.1175/1520-0469(1957)014<0115:RSORPM>2.0.CO;2.

Grell, G. A., and S. R. Freitas, 2014: A scale and aerosol aware stochastic convective parameterization for weather and air quality modeling. *Atmos. Chem. Phys.*, **14**, 5233–5250, https://doi.org/10.5194/acp-14-5233-2014.

Gultepe, I., M. D. Müller, and Z. Boybeyi, 2006: A new visibility parameterization for warm-fog applications in numerical weather prediction models. *J. Appl. Meteor. Climatol.*, **45**, 1469–1480, https://doi.org/10.1175/JAM2423.1.

——, and Coauthors, 2009: The fog remote sensing and modeling field project. *Bull. Amer. Meteor. Soc.*, **90**, 341–360, https://doi.org/10.1175/2008BAMS2354.1.

——, and Coauthors, 2016: An overview of the MATERHORN Fog Project: Observations and predictability. *Pure Appl. Geophys.*, **173**, 2983–3010, https://doi.org/10.1007/s00024-016-1374-0.

——, and Coauthors, 2021: A review of coastal fog microphysics during C-FOG. *Bound.-Layer Meteor.*, **181**, 227–265, https://doi.org/10.1007/s10546-021-00659-5.

Hersbach, H., and Coauthors, 2023: ERA5 hourly data on pressure levels from 1940 to present. Copernicus Climate Change Service (C3S) Climate Data Store (CDS), accessed 5 June 2023, https://doi.org/10.24381/cds.adbb2d47.

Hintz, T. J., and Coauthors, 2024: A mechanism for coastal fog genesis at evening transition. *Quart. J. Roy. Meteor. Soc.*, **150**, 2727–2743, https://doi.org/10.1002/qj.4732.

Hodur, R. M., 1997: The Naval Research Laboratory's Coupled Ocean/Atmosphere Mesoscale Prediction System (COAMPS). *Mon. Wea. Rev.*, **125**, 1414–1430, https://doi.org/10.1175/1520-0493(1997)125<1414:TNRLSC>2.0.CO;2.

Hong, S. Y., Y. Noh, and J. Dudhia, 2006: A new vertical diffusion package with an explicit treatment of entrainment processes. *Mon. Wea. Rev.*, **134**, 2318–2341, https://doi.org/10.1175/MWR3199.1.

Huang, S., W. Hu, J. Chen, Z. Wu, D. Zhang, and P. Fu, 2021: Overview of biological ice nucleating particles in the atmosphere. *Environ. Int.*, **146**, 106197, https://doi.org/10.1016/j.envint.2020.106197.

Isaac, G. A., T. Bullock, J. Beale, and S. Beale, 2020: Characterizing and predicting marine fog offshore Newfoundland and Labrador. *Wea. Forecasting*, **35**, 347–365, https://doi.org/10.1175/WAF-D-19-0085.1.

Jiménez, P. A., J. Dudhia, J. F. Gonzalez-Rouco, J. Navarro, J. P. Montavez, and E. Garcia-Bustamante, 2012: A revised scheme for the WRF surface layer formulation. *Mon. Wea. Rev.*, **140**, 898–918, https://doi.org/10.1175/MWR-D-11-00056.1.

Jumper, E. J., and S. Gordeyev, 2017: Physics and measurement of aero-optical effects: Past and present. *Annu. Rev. Fluid Mech.*, **49**, 419–441, https://doi.org/10.1146/annurev-fluid-010816-060315.

Jung, J., H. Furutani, M. Uematsu, S. Kim, and S. Yoon, 2013: Atmospheric inorganic nitrogen input via dry, wet, and sea fog deposition to the subarctic western North Pacific Ocean. *Atmos. Chem. Phys.*, **13**, 411–428, https://doi.org/10.5194/acp-13-411-2013.

Karimi, M., 2020: Direct numerical simulation of fog: The sensitivity of a dissipation phase to environmental conditions. *Atmosphere*, **11**, 12, https://doi.org/10.3390/atmos11010012.

Kecorius, S., and Coauthors, 2023: Rapid growth of Aitken-mode particles during Arctic summer by fog chemical processing and its implication. *PNAS Nexus*, **2**, 124, https://doi.org/10.1093/pnasnexus/pgad124.

Kit, E., C. M. Hocut, D. Liberzon, and H. J. S. Fernando, 2017: Fine-scale turbulent bursts in stable atmospheric boundary layer in complex terrain. *J. Fluid Mech.*, **833**, 745–772, https://doi.org/10.1017/jfm.2017.717.

Knopf, D. A., P. A. Alpert, and B. Wang, 2018: The role of organic aerosol in atmospheric ice nucleation: A review. *ACS Earth Space Chem.*, **2**, 168–202, https://doi.org/10.1021/acsearthspacechem.7b00120.

Köhler, H., 1936: The nucleus in and the growth of hygroscopic droplets. *Trans. Faraday Soc.*, **32**, 1152–1161, https://doi.org/10.1039/TF9363201152.

Koračin, D., and C. E. Dorman, Eds., 2017: *Marine Fog: Challenges and Advancements in Observations, Modeling, and Forecasting.* Springer, 537 pp.

——, J. Lewis, W. T. Thompson, C. E. Dorman, and J. A. Businger, 2001: Transition of stratus into fog along the California coast: Observations and modeling. *J. Atmos. Sci.*, **58**, 1714–1731, https://doi.org/10.1175/1520-0469(2001)058<1714:TOSIFA>2.0.CO;2.

——, C. E. Dorman, J. M. Lewis, J. G. Hudson, E. M. Wilcox, and A. Torregrosa, 2014: Marine fog: A review. *Atmos. Res.*, **143**, 142–175, https://doi.org/10.1016/j.atmosres.2013.12.012.

Lakra, K., and K. Avishek, 2022: A review on factors influencing fog formation, classification, forecasting, detection and impacts. *Rend. Lincei Sci. Fis. Nat.*, **33**, 319–353, https://doi.org/10.1007/s12210-022-01060-1.

Leipper, D. F., 1994: Fog on the U.S. West Coast: A review. *Bull. Amer. Meteor. Soc.*, **72**, 229–240, https://doi.org/10.1175/1520-0477(1994)075<0229:FOTUWC>2.0.CO;2.

Lozovatsky, I., C. Wainwright, E. Creegan, and H. J. S. Fernando, 2021: Ocean turbulence and mixing near the shelf break southeast of Nova Scotia. *Bound.-Layer Meteor.*, **181**, 425–441, https://doi.org/10.1007/s10546-020-00576-z.

MacDonald, M., M. J. Kurowski, and J. Teixeira, 2020: Direct numerical simulation of the moist stably stratified surface layer: Turbulence and fog formation. *Bound.-Layer Meteor.*, **175**, 343–368, https://doi.org/10.1007/s10546-020-00511-2.

Mansell, E. R., C. L. Ziegler, and E. C. Bruning, 2010: Simulated electrification of a small thunderstorm with two-moment bulk microphysics. *J. Atmos. Sci.*, **67**, 171–194, https://doi.org/10.1175/2009JAS2965.1.

Meng, Z., and J. H. Seinfeld, 1994: On the source of the submicrometer droplet mode of urban and regional aerosols. *Aerosol Sci. Technol.*, **20**, 253–265, https://doi.org/10.1080/02786829408959681.

Mlawer, E. J., S. J. Taubman, P. D. Brown, M. J. Iacono, and S. A. Clough, 1997: Radiative transfer for inhomogeneous atmospheres: RRTM, a validated correlated-k model for the longwave. *J. Geophys. Res.*, **102**, 16 663–16 682, https://doi.org/10.1029/97JD00237.

Myers, J. N., 1968: Fog. *Sci. Amer.*, **219**, 74–83.

Nakanishi, M., 2000: Large-eddy simulation of radiation fog. *Bound.-Layer Meteor.*, **94**, 461–493, https://doi.org/10.1023/A:1002490423389.

——, and H. Niino, 2006: An improved Mellor_Yamada Level-3 model: Its numerical stability and application to a regional prediction of advection fog. *Bound.-Layer Meteor.*, **119**, 397–407, https://doi.org/10.1007/s10546-005-9030-8.

Niece, M., and C. Kaiser, 2018: Directed energy outreach. *Proc. Directed Energy Educational Outreach Campaign*, Directed Energy Professional Society, 11 pp., https://www.deps.org/DEPSpages/DEoutreach.html.

NWS, 2024: Super fog. Accessed 25 April 2024, https://www.weather.gov/safety/fog-super.

Ortiz-Suslow, D., and Coauthors, 2025: A case study of boundary-layer development downstream of a small, remote island. *Quart. J. Roy. Meteor. Soc.*, **151**, e4929, https://doi.org/10.1002/qj.4929.

Pawlak, R. J., 2012: Recent developments and near term directions for Navy laser weapons system (LaWS) testbed. *Proc. SPIE*, **8547**, 854705, https://doi.org/10.1117/12.976031.

Perram, G. P., S. J. Cusumano, R. L. Hengehold, and S. T. Fiorino, 2010: *An Introduction to Laser Weapon Systems.* Directed Energy Professional Society, 463 pp.

Place, B. K., C. J. Young, S. E. Ziegler, K. A. Edwards, L. Salehpoor, and T. C. VandenBoer, 2018: Passive sampling capabilities for ultra-trace quantitation of atmospheric nitric acid (HNO3) in remote environments. *Atmos. Environ.*, **191**, 360–369, https://doi.org/10.1016/j.atmosenv.2018.08.030.

Poku, C., A. N. Ross, A. M. Blyth, A. A. Hill, and J. D. Price, 2019: How important are aerosol–fog interactions for the successful modelling of nocturnal radiation fog? *Weather*, **74**, 237–243, https://doi.org/10.1002/wea.3503.

Pollard, R., P. Rhines, and R. Thompson, 1972: The deepening of the wind-mixed layer. *Geophys. Fluid Dyn.*, **4**, 381–404, https://doi.org/10.1080/03091927208236105.

Pruppacher, H. R., and J. D. Klett, 2010: Microstructure of atmospheric clouds and precipitation. *Microphysics of Clouds and Precipitation*, Springer, 10–73.

Pu, Z., and Coauthors, 2023: Cold fog amongst complex terrain. *Bull. Amer. Meteor. Soc.*, **104**, E2030–E2052, https://doi.org/10.1175/BAMS-D-22-0030.1.

Richter, D. H., T. MacMillan, and C. Wainwright, 2021: A Lagrangian cloud model for the study of marine fog. *Bound.-Layer Meteor.*, **181**, 523–542, https://doi.org/10.1007/s10546-020-00595-w.

Rodhe, B., 1962: The effect of turbulence on fog formation. *Tellus*, **14**, 49–86, https://doi.org/10.3402/tellusa.v14i1.9528.

Salehpoor, L., and T. C. VandenBoer, 2023: Suppressor and calibration standard limitations in cation chromatography of ammonium and 10 alkylamines in atmospheric samples. *Anal. Methods*, **15**, 3822–3842, https://doi.org/10.1039/D3AY01158E.

Sasakawa, M., A. Ooki, and M. Uematsu, 2003: Aerosol size distribution during sea fog and its scavenge process of chemical substances over the northwestern North Pacific. *J. Geophys. Res.*, **108**, 4120, https://doi.org/10.1029/2002JD002329.

Schiffer, J. M., L. E. Mael, K. A. Prather, R. E. Amaro, and V. H. Grassian, 2018: Sea spray aerosol: Where marine biology meets atmospheric chemistry. *ACS Cent. Sci.*, **4**, 1617–1623, https://doi.org/10.1021/acscentsci.8b00674.

Shin, H. H., and S. Y. Hong, 2015: Representation of the subgridscale turbulent transport in convective boundary layers at gray-zone resolutions. *Mon. Wea. Rev.*, **143**, 250–271, https://doi.org/10.1175/MWR-D-14-00116.1.

Singh, D. K., S. W. Hoch, I. Gultepe, and E. R. Pardyjak, 2024: A case study of the life cycle of a stratus-lowering coastal-fog event in Newfoundland, Canada. *Quart. J. Roy. Meteor. Soc.*, **150**, 641–662, https://doi.org/10.1002/qj.4615.

Skamarock, W. C., and Coauthors, 2008: A description of the Advanced Research WRF version 3. NCAR Tech. Note NCAR/TN-475+STR, 113 pp., https://doi.org/10.5065/D68S4MVH.

Soveizi, N., A. M. Latifi, S. Mehrabian, and A. Akhavan Sepahi, 2023: Bacterial ice nucleation proteins: Features, structure, and applications. *J. Appl. Biotechnol. Rep.*, **10**, 1041–1054, https://doi.org/10.30491/jabr.2022.328815.1495.

Spirig, R., and Coauthors, 2019: Probing the fog life cycles in the Namib Desert. *Bull. Amer. Meteor. Soc.*, **100**, 2491–2507, https://doi.org/10.1175/BAMS-D-18-0142.1.

Taylor, G. I., 1917: The formation of fog and mist. *Quart. J. Roy. Meteor. Soc.*, **43**, 241–268, https://doi.org/10.1002/qj.49704318302.

Theethai Jacob, A., and Coauthors, 2023: Implementation of the urban parameterization scheme in the Delhi model with an improved urban morphology. *Quart. J. Roy. Meteor. Soc.*, **149**, 40–60, https://doi.org/10.1002/qj.4382.

Torregrosa, A., T. A. O'Brien, and I. C. Faloon, 2014: Coastal fog, climate change, and the environment. *Eos, Trans. Amer. Geophys. Union*, **95**, 473–474, https://doi.org/10.1002/2014EO500001.

Van der Hoven, I., 1957: Power spectrum of horizontal wind speed in the frequency range from 0.0007 to 900 cycles per hour. *J. Meteor.*, **14**, 160–164, https://doi.org/10.1175/1520-0469(1957)014<0160:PSOHWS>2.0.CO;2.

Van der Velde, I. R., G. J. Steeneveld, B. W. Schreur, and A. A. M. Holtslag, 2010: Modeling and forecasting the onset and duration of severe radiation fog under frost conditions. *Mon. Wea. Rev.*, **138**, 4237–4253, https://doi.org/10.1175/2010MWR3427.1.

Vladimirov, E., R. Dimitrova, and V. Danchovski, 2018: Sensitivity of WRF Model results to topography and land cover: Study for the Sofia Region. *Annu. Sofia*, **111**, 87–101.

Wagh, S., R. Krishnamurthy, C. Wainwright, S. Wang, C. E. Dorman, H. J. S. Fernando, and I. Gultepe, 2021: Study of stratus-lowering marine-fog events observed during C-FOG. *Bound.-Layer Meteor.*, **181**, 317–344, https://doi.org/10.1007/s10546-021-00670-w.

WMO, 1992: *International Meteorological Vocabulary.* WMO, 782 pp.

Wu, S., and Coauthors, 2022: Particle number size distribution of PM_1 and PM_{10} in fogs and implications on fog droplet evolutions. *Atmos. Environ.*, **277**, 119086, https://doi.org/10.1016/j.atmosenv.2022.119086.

Yamaguchi, R., and Coauthors, 2025: A shipboard atmospheric surface layer profiling system for air-sea interaction and fog studies. *Quart. J. Roy. Meteor. Soc.*, in press.

Zhao, S., and Coauthors, 2022: Changes in aerosol particle composition during sea fog formation events in the sea ice regions of the Arctic Ocean. *Atmos. Environ.*, **272**, 118943, https://doi.org/10.1016/j.atmosenv.2022.118943.